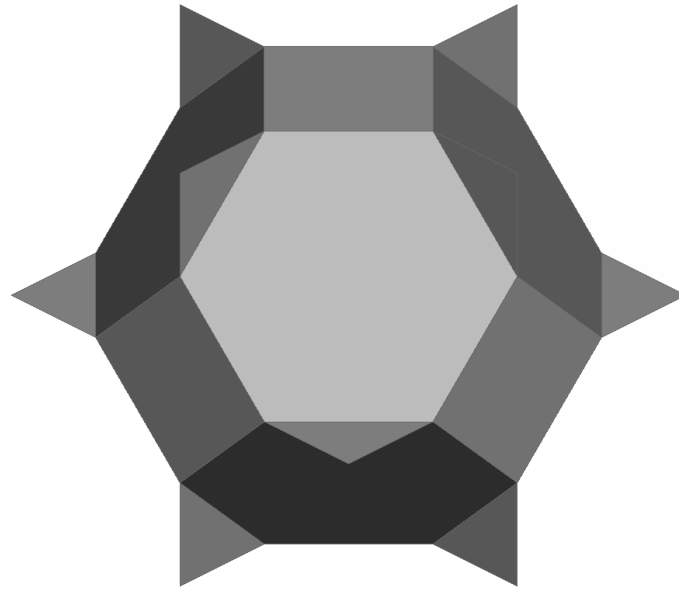




CHALMERS



Modelling the mechanical response of cellular PVC foams using detailed finite element analysis

Master's thesis in Applied Mechanics

Rikard Berg
Adam Billberg

2019

Department of Industrial and Materials Science
CHALMERS UNIVERSITY OF TECHNOLOGY
Göteborg, Sweden 2019

Master's thesis in applied mechanics
2019

**Modelling the mechanical response of cellular PVC foams using detailed finite
element analysis**

Rikard Berg
Adam Billberg



CHALMERS
UNIVERSITY OF TECHNOLOGY

Department of Industrial and Materials Science
Division of Material and Computational Mechanics
CHALMERS UNIVERSITY OF TECHNOLOGY
Göteborg, Sweden 2019

Modelling the mechanical response of cellular PVC foams using detailed finite element analysis
RIKARD BERG
ADAM BILLBERG

©RIKARD BERG, ADAM BILLBERG, 2019

Master's thesis 2019
Department of Industrial and Materials Science
Division of Material and Computational Mechanics
Chalmers University of Technology
SE-412 96 Göteborg
Sweden
Telephone: +46 31 772 10 00

Cover: Tetrakaidecahedron used as Repetitive Volume Element to emulate foam

Chalmers Reproservice
Göteborg, Sweden 2019

Abstract

The use of composites with a foam core is becoming more and more common as industries strive to make lighter structures. However, the mechanical response of cellular foams is hard to model properly due to its complicated microstructure and deformation mechanisms. Previous work in the field of modelling cellular foams have focused on capturing the yield surface using both advanced material models and by modelling the microstructure of the foam. The current study aims at capturing the macroscale stress-strain response during uniaxial tension, compression, and shear loads by performing analyses on a geometry representing the foam microstructure. Two foams are investigated in the current study; Divinycell H60 and H100, manufactured by Diab.

The Kelvin tetrakaidecahedron was used to represent the foam microstructure of a single cell. The efficiency of the simulations were greatly enhanced by the use of a Representative Volume Element (RVE) with Periodic Boundary Conditions (PBC) to emulate an infinitely large foam under constant average strain using a single foam cell. This allowed for calibration of key parameters through an iterative process, with the aim to capture the mechanical response for one of the investigated foams, Divinycell H100. Experimental results from the remaining foam, Divinycell H60, was then used to validate the derived parameters without a separate optimisation procedure.

The study found that an RVE can be used to accurately model the initial mechanical response of foam in both the elastic and plastic region. By optimising material and geometric parameters for the H100 foam, the elastic region was captured well for both tension and shear in two principal directions. Furthermore, the compressive behaviour in the elastic region and the initial phase of buckling was captured in two principal directions. By using the same material parameters and re-scaling the geometric parameters, good correlations to the experimental data was achieved also for H60. Due to the progressive crushing at large compressive strains, cellular foams do not behave periodically in the direction of the load. This makes it impossible to capture the full true deformation mechanisms using full PBC's, since they imply that the material behaves periodically in all directions.

Keywords: PVC Foam, Representative Volume Element, Periodic Boundary Conditions, Finite Element Analysis, Divinycell, Microstructure.

Preface

The current project was conducted as a 30 credits Master's thesis project at Chalmers University of Technology during the spring of 2019. The authors, Rikard Berg and Adam Billberg, were both students at the master's program Applied Mechanics with Bachelor of Science degrees in Mechanical Engineering.

Acknowledgements

This project has been greatly supported by FS Dynamics, the consulting firm where the project was conducted. We would like to thank our supervisor at FS Dynamics, Dr. Rickard Juntikka, for his guidance, expertise, and help throughout the project. Furthermore, we would like to extend our gratitude to our examiner Assoc. Prof. Martin Fagerström for his encouragement and thoughtful advice throughout the project. Also a big thank you to the colleagues at FS Dynamics for their genuine interest in the project and their helpfulness. We would also like to thank M.Sc. Carl-Johan Lindholm at Diab for providing data on their foams and assisting us with his expertise in the field.

Abbreviations

ASA	Adaptive Simulated Annealing
BSE	Backscattering Electron
CAE	Computer Aided Engineering
DoF	Degree of Freedom
ESEM	Environmental Scanning Electron Microscope
FE	Finite Element
FEA	Finite Element Analysis
FEM	Finite Element Method
GSED	Gaseous Secondary Electron Detector
LFOP	Leapfrog Optimisation
PBC	Periodic Boundary Condition
PVC	Polyvinyl Chloride
RMS	Root Mean Square
RVE	Representative Volume Element

Nomenclature

Foam parameters

ν^*	Macroscale Poisson's ratio	—
ϕ	Fraction of solid in cell edge	—
ρ^*	Macroscale density	kg/m ³
ρ_s	Density of bulk material	kg/m ³
ρ_{rel}	Relative density	—
σ_{pl}^*	Macroscale yield stress	Pa
σ_{ys}	Yield stress of bulk material	Pa
A_{RVE}	Surface area in the RVE	m ²
E^*	Macroscale Young's modulus	Pa
E_s	Young's modulus	Pa
G^*	Macroscale shear modulus	Pa
G_s	Shear modulus of bulk material	Pa
H_s	Isotropic hardening modulus of bulk material	Pa
L	Elongation factor of the foam cell	m
t	Thickness of shell elements	m
V_{RVE}	Volume of the RVE	m ³

Arc length method

$\Delta\lambda$	Load proportionality factor	—
$\Delta\mathbf{u}$	Incremental displacement	m
Δl	Arc length	m
Ψ	Relation between load- and displacement increment	—
\mathbf{F}^{int}	Internal force vector	N
\mathbf{q}	External force vector	N
\mathbf{R}	Residual	N

Other Symbols

σ	Stress	Pa
γ	Shear angle	—
h	Height of RVE	m
ϵ^0	Applied global strain	—
F	Reaction force	N

A	Area normal to applied load	m^2
e	Engineering strain	—
l	Current length of RVE	m
l_0	Initial length of RVE	m
\hat{u}	Dummy node displacement	m
u	Nodal displacement	m
τ	Shear stress	Pa

Contents

Abstract	i
Preface	iii
Acknowledgements	iii
Abbreviations	v
Nomenclature	vii
1 Introduction	1
1.1 Background	1
1.2 Aim	2
1.3 Method	2
1.4 Limitations	2
2 Theory	3
2.1 Manufacturing of Divinycell	3
2.2 Physical properties of foams	3
2.2.1 Experimental data	4
2.3 The creation of the foam microstructure	5
2.4 Geometric models for foam materials	5
2.4.1 Kelvin structure	6
2.4.2 Weaire-Phelan structure	7
2.4.3 Stochastically generated models	7
2.5 Commercially available material models for foam materials	8
2.6 Arc Length Method - Riks analysis	8
3 Method	11
3.1 FEM implementation of RVE	11
3.1.1 Periodic Boundary Conditions	11
3.1.2 PBC implementation in Abaqus	13
3.1.3 Verification of the PBC's	14
3.2 Analysis setup	14
3.2.1 Geometry and Material	14
3.2.2 Boundary conditions and loads	15
3.2.3 Analysis	16
3.2.4 Buckling initiation	16
3.3 Meshing of Geometry	17
3.4 Foam microstructure study	18
3.4.1 Specimen preparation	19
3.4.2 Image retrieval	19
3.4.3 Image analysis	19
3.5 Parameter optimisation using LS-OPT	20
3.5.1 LS-OPT setup	21

3.6	Re-scaling of geometric parameters to the H60 foam	22
3.7	Calculation of global material parameters	23
4	Results	25
4.1	ESEM study	25
4.2	Optimisation of mechanical behaviour	26
4.2.1	H100 Uniaxial strain analyses	27
4.2.2	H100 Uniaxial stress analyses	28
4.2.3	H60 Uniaxial stress analyses	30
4.2.4	Buckling deformation	32
4.2.5	Global material parameters	32
5	Discussion	35
5.1	ESEM study	35
5.2	Derived bulk and global parameters	35
5.3	Deformation mechanics	36
5.4	Element type	37
5.5	Error sources	37
5.5.1	Analysis type	37
5.5.2	Influence of imperfection	37
5.5.3	Incorrect boundary conditions for shear analyses	39
6	Conclusions	41
7	Future work	43
	Appendix	i
A.1	PBC Matlab code	i
A.2	Python code used to extract stresses and strains	v
A.3	Example input file	vi
A.4	Images from ESEM microstructure study	viii

Introduction

Product development have in a large quantity of fields long been striving to make lighter and stronger components, which has made composite structures popular. To build volume in these structures, cellular foams have been utilised as it is light weight and sufficiently stiff to carry the internal loads of the composite structures. Examples of fields where foam cores are currently being used are transport, marine, and aerospace industry, as lighter structures in these fields lead to reduced fuel consumption. Since the safety of human lives often must be certified in these industries, the mechanical response of all included materials must be known in order to optimise the reduction of weight while maintaining a tolerable safety factor. It is therefore of high importance to be able to model the mechanical behaviour of not only the load carrying composite, but also the volume building cellular foam.

Previous works in the field of modelling cellular foams have focused on developing advanced material models that adequately capture the mechanical behaviour of cellular foams. Furthermore, Finite Element (FE) models of geometries representing single or multiple foam cells have been used to capture the yield surface of foams and to validate material models.

The current study aims not to capture the yield surface of cellular foams but rather the stress-strain behaviour by performing simulations on a geometry representing the foam cell structure. The mechanical response should be captured using an as simple material model as possible, while the deformation of the geometry causes the more advanced average stress-strain behaviour. The project focuses on the closed cell foams Divinycell H60 and H100 manufactured by Diab¹.

1.1 Background

FS Dynamics² have conducted several projects with Computer Aided Engineering (CAE) of foams and have concluded that the readily available material models used in commercial FE codes, e.g. Abaqus or LS Dyna, do not describe the material behaviour in a satisfactory manner. Therefore, this thesis has been proposed to further study the material and develop an FE model that adequately demonstrates the behaviour and general stress-strain relationship of foam materials.

Attempts to capture the mechanical response of foams through geometric structures have previously been done by e.g. Ayyagari et al. [1–3] using Timoshenko beam elements to build a lattice structure representing cell edges of an open foam structure, and by Daxner et al. [4] who modelled the cells with shell elements to emulate a closed cell foam. Both works, however, focus on achieving a good correlation of the yield surfaces between the FE model and a proposed material model, and later also validating the yield surface with experimental data.

The current study aims to capture the stress-strain response of cellular foams, up to a predefined strain, by modelling the microstructure of the foam. Due to the manufacturing process of Divinycell foams, accurate material parameters of the bulk material, i.e. the material the cell walls are comprised of, are hard to determine. These parameters will be estimated through an iterative process and presented in the report. To have an as accurate approximation of the geometry of the cells as possible, a study on the geometry of the microstructure is also conducted, and data of cell shape and size in the

¹Diab is a manufacturer of high-performance core materials.

² FS Dynamics is a focused and independent consultancy company providing highly skilled competence within fluid- and structural dynamic analysis.

through-thickness direction is investigated.

1.2 Aim

The primary goal of the project is to develop a finite element model of a geometry representing a foam microstructure that adequately captures the true mechanical response of Divinycell H60 and H100 under uniaxial stress loads. The model should capture the initial linearly elastic behaviour and subsequent nonlinear behaviour of foams in compression, tension, and shear.

1.3 Method

To better understand foam materials, a literature study is conducted. The study presents the current material models as well as previous geometric FE models used to model open and closed cell foams. It discusses the strengths and weaknesses of the models and provides a good basis for the project to start from.

The material behaviour is captured through FE simulations performed on a geometry representing the foam microstructure, modelled as a Representative Volume Element (RVE). To capture the macroscale behaviour of foam, Periodic Boundary Conditions (PBC) are used to emulate that the RVE is periodically repeated in all directions and subjected to a constant average strain. The RVE used to represent the foam is created according to how a cluster of bubbles would be arranged in relation to each other, with the condition that all bubbles were of the same size.

Due to the lack of readily available data on the microstructure of the studied foams, H60 and H100, a study on their microstructure is conducted. An Environmental Scanning Electron Microscope (ESEM) is used to capture images of the foam microstructure in several layers through the thickness of the foam, and image processing is used to determine the sizes and shapes of the cells.

When the size and shape of the cells are known, the FE model is calibrated such that the captured stress-strain behaviour of the model coincides with experimental data for H100. The calibrated parameters from H100 are then validated through analyses on H60. The resulting FE model should therefore accurately represent the foam microstructure and properly capture the stress-strain behaviour of the two foam materials.

1.4 Limitations

Regarding the time frame of the project, it is conducted as a 30 credit thesis work at Chalmers University of Technology which implies that the limiting time frame of the project is 20 weeks, or 800 hours. The project will focus on Divinycell H60 and H100 and therefore the method is developed for these specific foams. Furthermore, the method is developed for Abaqus, which is the FE code that will be used for all analyses.

Mechanical testing of foams is not included in the scope of the project, as data will be provided by Diab. The well established phenomenon of densification [5], the stage where the cells have collapsed and the material starts to densify, will not be modelled. This is due to the complex microscopic behaviour at this stage which requires a large amount of contact points to be established inside the cells, increasing the solution times and impairing convergence. Therefore, no focus will be put on this phenomenon. The project will be limited to only model the initial elastic and plastic behaviour of the foam.

Finally, the use of a single RVE with PBC's implies that all cells in the foam deforms in the same manner and at the same time. Large compressive strains, where the foam microstructure begins to buckle layer by layer, can therefore not be analysed.

2

Theory

In the following chapter a more detailed introduction of foams is given and some previous works on the modelling of foams are introduced. Furthermore, some general theories behind the FE analyses used are described.

2.1 Manufacturing of Divinycell

Diabs Divinycell polyvinyl chloride (PVC) foams are manufactured by first mixing the raw ingredients and pouring them into a mold. The mold is then clamped shut and placed in a large press where it is heated. After this process the foam is in the form of a solid slab. It is then placed in a hot bath where it is allowed to expand in its thickness direction until it reaches its final density and is cured. It is this process that causes the elongation of the foam cells. Finally, the foams are cut into sheets according to the customer specifications. [6]

2.2 Physical properties of foams

Due to the inherent microscopic structure of foams, the global stress-strain behaviour is complicated. In compression, see Figure 2.1a, foam materials behave linearly elastic until initial yield occurs. After yielding, microscopic buckling of the cell walls starts in one layer. This leads to progressive crushing as the cells buckle layer by layer creating the crushing regime where a stress plateau is observed. This continues until all cells have buckled upon which densification begins [7, 8]. In tension the material behaves as a brittle material [8, 9], see Figure 2.1b.

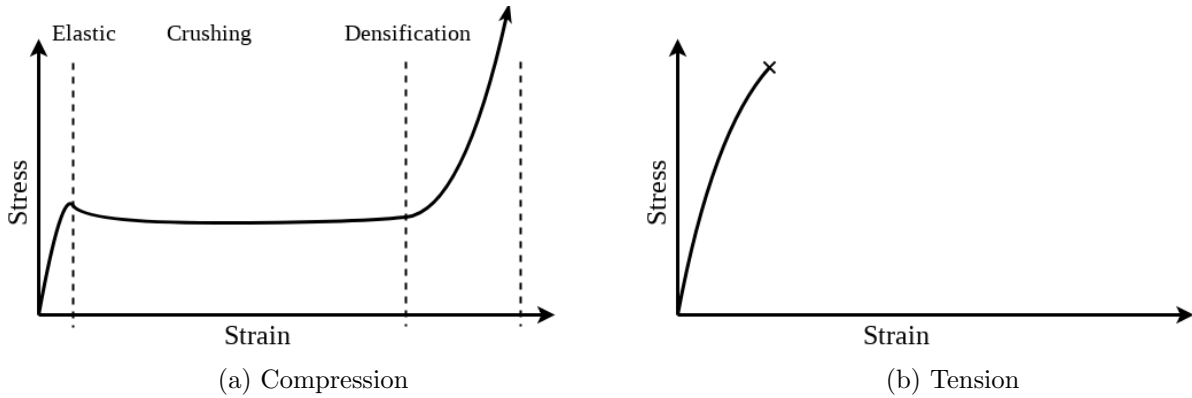


Figure 2.1: General stress-strain behaviour of closed cell foams

Divinycell foams have also been found to be transversely isotropic, further complicating the modelling [8]. The transversely isotropic property arise from the manufacturing process in which the size of the cells grow more in the *rise direction* of the foam, referred to as the through-thickness direction (3). The plane orthogonal to this direction is referred to as the plane of isotropy (1-2), see Figure 2.2. In the planes 1-3 and 2-3, each with a normal in the two other principal directions, the elongation of the foam cells can be observed, creating two planes of anisotropy.

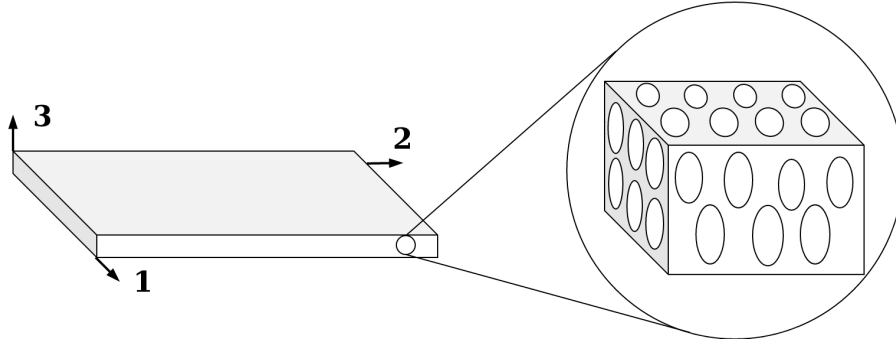


Figure 2.2: Illustration of foam microstructure

Because the thickness of each cell wall is excessively thin, they are hard to measure. One study, using image analysis, done by Colloca et al. [10], found that the mean thickness of the cell walls for both H60 and H100 was $8\text{ }\mu\text{m}$ with a standard deviation of $3\text{ }\mu\text{m}$ and $4\text{ }\mu\text{m}$ respectively. The thickness can also be estimated from the relative density of the foam and the density of the bulk material, assuming that the material is evenly distributed in the foam¹.

The mechanical behaviour of foams is influenced by the fraction of material in the so-called Plateau borders. This distribution of material was studied by Simone and Gibson [11] on metallic foams by using shell and solid elements and increasing the radius of the plateau border. It was concluded that shifting material to the plateau borders has marginal effects on the stiffness of the foam but causes a reduction of the peak stress. This effect was also studied using stochastic models by Köll and Hallström [12]. Instead of changing the curvature of the Plateau borders, they used a combination of shell elements for the faces and beam elements for the edges. The material fraction could then be investigated by relocating material from the shell elements to the beam elements. They concluded that the distribution of solid material between the cell faces and edges influences the relative elastic modulus and that the influence increases as the relative density increases.

2.2.1 Experimental data

The experimental stress-strain data aimed to be captured by the FE model are presented in Figures 2.3 and 2.4. This data was provided by Diab and obtained by subjecting foam test specimens to uniaxial stress according to ASTM D 1621, ASTM D 1623, and ISO 1922 for compression, tension, and shear respectively.

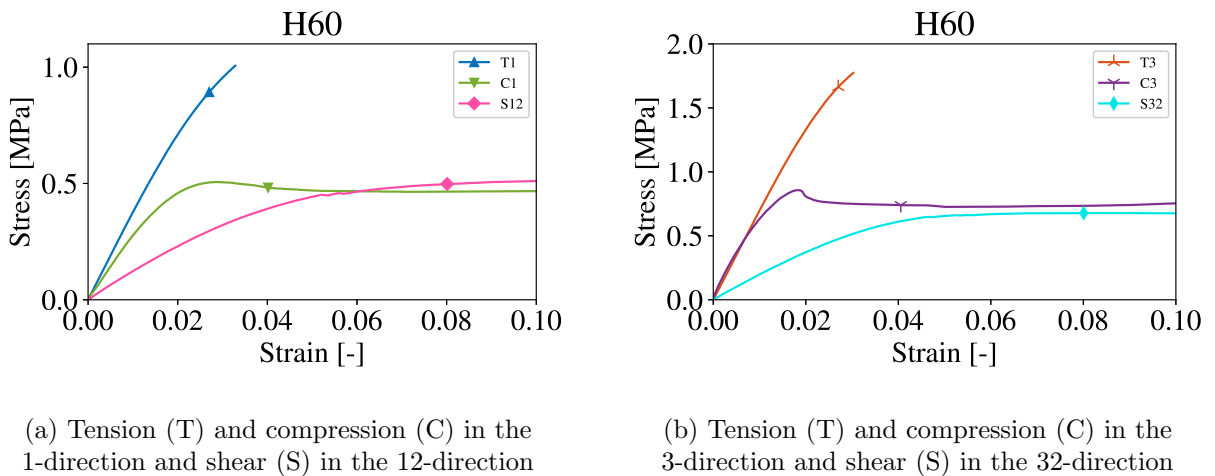


Figure 2.3: Experimental data for H60

¹This is explained further in Chapter 3

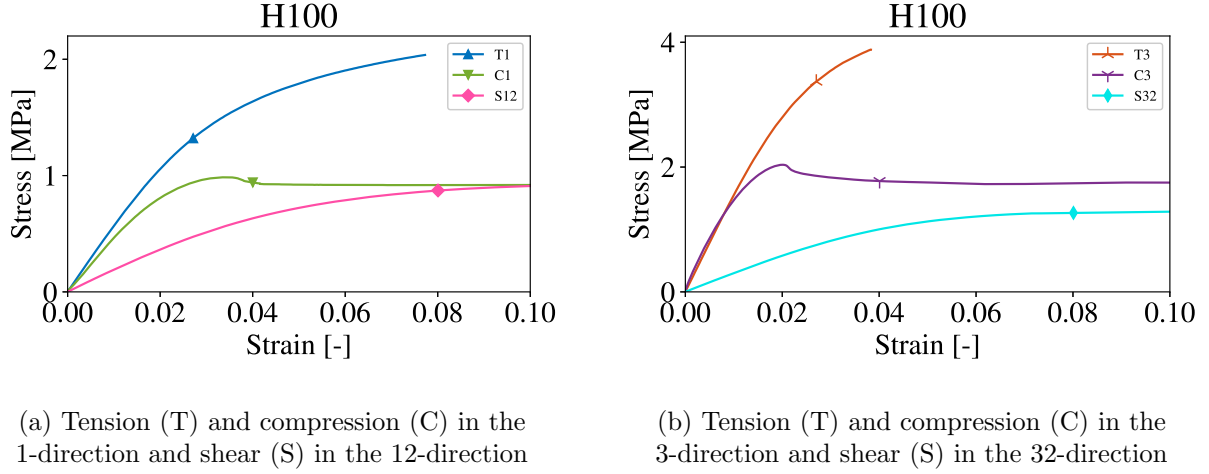


Figure 2.4: Experimental data for H100

2.3 The creation of the foam microstructure

The process in which cellular foams are manufactured involves a gas and a liquid in the form of a myriad of bubbles, wherein the liquid undergoes a phase change creating the solid structure. The natural behaviour of any cluster of liquid surfaces is to minimise the surface energy, following the rules recorded by Plateau [13] in 1873 and the Young-Laplace equation describing pressure difference over an interface in fluid mechanics. For two adjacent liquid cells with the same internal pressure the dividing surface of the cells must have a zero mean curvature. In the junction lines where three cells meet the laws of Plateau state that the angle between the surfaces must be 120° , implying also that only three cells may intersect at a time. The laws of Plateau further state that only four junction lines may meet at a time, creating vertices, and they must do so at perfectly symmetrically forming angles of 109.47° between each border line.

When the foam is in its liquid phase, the evolution of the structure depends on the surface tension in the faces and the drainage, how the liquid material flows throughout the structure, of the foam. For foams with low drainage, a large amount of the liquid is confined to the junction lines between three faces, creating so called Plateau borders [4]. When the liquid solidifies these Plateau borders make up load carrying struts. Foams with a lower content of fluid have less profound Plateau borders, making the edges of the cells an area of interest when modelling the stiffness of the cellular foam. Simone and Gibson [11] suggest that the influence of the Plateau border in the Young's modulus and plastic collapse stress of foams can be estimated by the factor ϕ according to the equations

$$\frac{E^*}{E_S} = (1 - \phi)\rho_{\text{rel}} + \phi\rho_{\text{rel}}^2 \quad (2.1)$$

$$\frac{\sigma_{\text{pl}}^*}{\sigma_{\text{YS}}} = (1 - \phi)\rho_{\text{rel}} + 0.3\phi\rho_{\text{rel}}^{3/2} \quad (2.2)$$

$$\rho_{\text{rel}} = \frac{\rho^*}{\rho_S} \quad (2.3)$$

where ϕ is the fraction of solid contained in the cell edge. Introduced here are also the ratios between the modulus, density, and plastic collapse stress for the global foam material on the macroscale (E^* , ρ^* , σ_{pl}^*) and the local solid bulk material on the microscale (E_S , ρ_S , σ_{YS}).

2.4 Geometric models for foam materials

Bubbles created by the laws stated in Section 2.3 will differ in size and shape. A simplification of the structure is therefore desirable for modelling purposes. One possible simplification is to use a

symmetric unit cell with as low surface energy as possible to approximate the cell structure of the foam. One such repeatable unit cell widely implemented in research is the Kelvin structure, derived in 1887 by Lord Kelvin [14]. The Kelvin unit cell was beaten, with 0.3% less surface energy per unit volume, in 1993 by Denis Weaire and Robert Phelan with the Weaire-Phelan structure [15]. While the Kelvin structure is considered the first step to understand foam [1], the Weaire-Phelan structure is less explored due to the fact that the improvement in mechanical properties for this more complicated structure has been shown to be nearly negligible [4]. The most recent research also includes creating completely stochastic foam models [12] resulting in a computationally more demanding problem. All three alternatives are described in more detail below.

2.4.1 Kelvin structure

A common way of modelling foams is to use the Kelvin tetrakaidecahedron, see Figure 2.5. This structure was proposed by lord Kelvin in 1887 [14] as the way to most efficiently divide space with minimum partitional area. Interestingly, lord Kelvin stated “This problem is solved in foam” in the opening paragraph as to how the solution of dividing space with minimum partitional area was devised, suggesting a strong link between the structure of foam and the Kelvin structure.

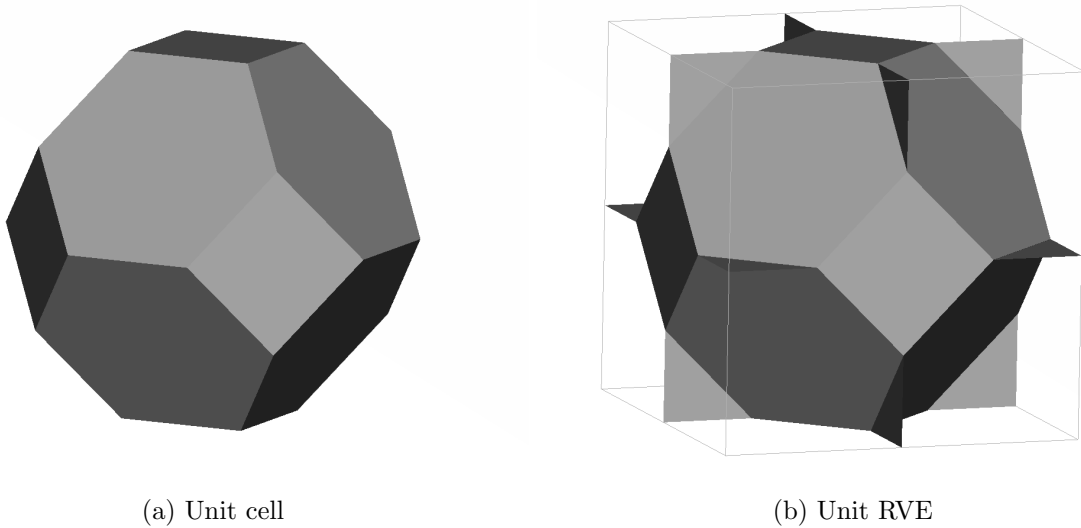


Figure 2.5: Kelvin Tetrakaidecahedron

The Kelvin structure was modelled using Timoshenko beams by Ayagari and Vural [1] to capture the yield surface of cellular foams. It was found that the yield surface from their FE model during a variety of loading scenarios coincided well with their newly proposed yield criterion [2] in which a linear pressure dependence had been introduced. Furthermore, they also state that periodic Kelvin models should be used with caution when modelling the behaviour after initial yield due to the instability that governs the following stress-strain response.

Daxner et al. [4] used periodical unit-cells modelled with shell elements to represent the cellular material and studied the yield behaviour when altering the relative density of the foam material. It was found that the Kelvin unit cell introduced a degree of anisotropy to the macro-scale elastic modulus E^* . This influence was then determined to be greater at low relative densities. Furthermore, they concluded that for relative densities below 0.05 the natural curvature of the cell walls should be modelled.

2.4.2 Weaire-Phelan structure

The Weaire-Phelan structure is comprised of two different cells that when combined creates the geometries seen in Figure 2.6. Even though the Weaire-Phelan unit cell is the lowest surface energy unit cell yet discovered [11] it is not widely used to model foams. A reason for this could be that it only has a slightly lower surface energy than the more established Kelvin structure while being more irregular, making it more cumbersome to work with. When comparing the two structures, Daxner et al. [4] found that the average mechanical properties are the same for the two structures within a few percent. Buffel et al. [16] points out that the Weaire-Phelan structure is mostly composed of pentagon cell faces, which are also abundant in real foam structures, concluding that the Weaire-Phelan structure represents the topology of real foam better. In the same study it is also concluded that the only major difference in mechanical response of open cell foams, modelled with Weaire-Phelan and Kelvin respectively, is that the former has a higher relative shear modulus, G^* , and a greater sensitivity to anisotropy. This is explained by the higher irregularity of the Weaire-Phelan structure.

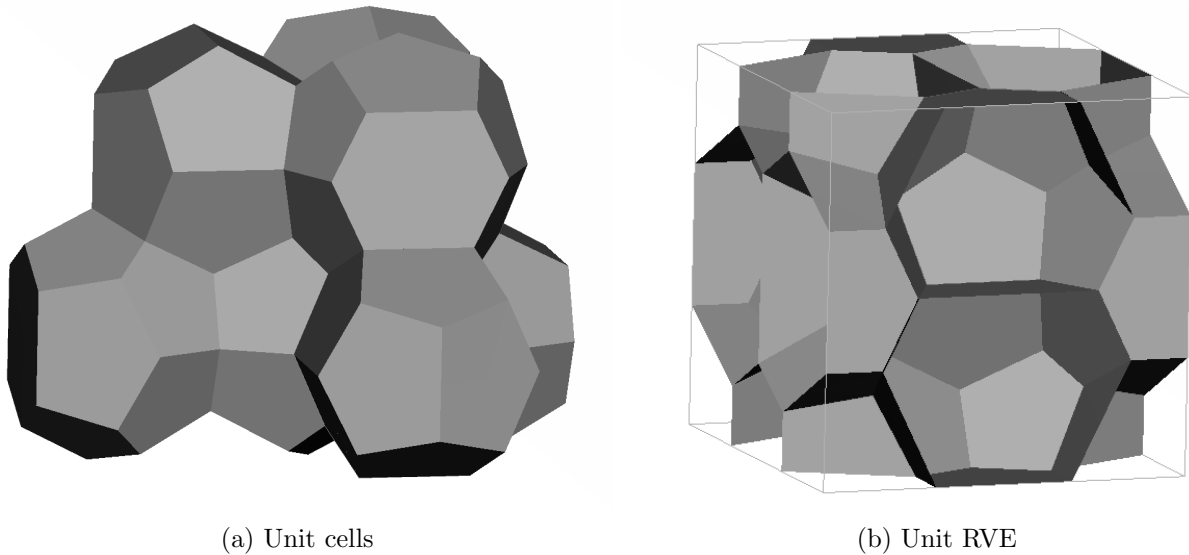


Figure 2.6: The Weaire-Phelan structure

2.4.3 Stochastically generated models

The structure of cellular foams is random; however, most attempts to model the mechanical behaviour use periodically repeatable unit cells. To evaluate the accuracy of these models it is also important to study randomly generated foam models. Garboczi and Roberts [17] studied two such models; one generated using Voronoi partitions and one generated using Gaussian random fields. It was found that the elastic modulus of the Voronoi model can be approximately described by the Kelvin model and that the Gaussian model was significantly less stiff than the Kelvin model due to the higher irregularity in the generated cell shapes.

Hallström and Köll [12] suggests a stochastic equilibrium FE foam model generated through Voronoi partitions enhanced using *Surface Evolver* [18] to reduce the surface energy of the generated cell structure. They conclude that models containing at least 85 randomly generated cells shows a relatively isotropic behaviour and that spread in cell volume has insignificant impact on the elastic properties. Furthermore they state that although the distribution of material in the cell walls has been found to have a significant impact on the elastic properties, it is challenging to model.

2.5 Commercially available material models for foam materials

Some material models exist in commercial FE codes, e.g. Abaqus and LS Dyna, that can be used to capture the behaviour of foams. However, these models usually have limitations and does not always yield accurate results.

Abaqus has three material models for foams: CRUSHABLE FOAM, HYPERFOAM, and LOW DENSITY FOAM [19]. The crushable foam material model is intended for crushable foams used for energy absorption, as it intends to model the compression of foams due to the cell wall buckling. Furthermore, it is also able to model the difference in behaviour in compression and tension and can utilise isotropic hardening for the plastic behaviour of the foam. However, it is only intended for monotonic loading and is purely isotropic. The second model, hyperfoam, is also only isotropic. Its primary use is for foams with large volumetric changes, up to 90% strain in compression, in nonlinear analyses. However, it is only elastic and requires experimental test data obtained from tests with similar deformation modes as the analysed problem as input to the material model. The final model, low density foam, is used for low density, highly compressible foams, with a rate sensitive behaviour. It requires stress-strain curves at different strain rates for both compression and tension and uses these curves to compute the stress by interpolation. If the computed strains are larger than the supplied data it uses the last data point and extrapolates the stress. It can also be used to model cyclic behaviour if the supplied data covers unloading. However, even if lateral strain data can be included to allow for the inclusion of Poisson effects it does not support negative Poisson effects.

LS Dyna has several material models that can be used to model foams, all with different characteristics and intended for different specific usage scenarios [20]. For example, MAT TRANSVERSELY ISOTROPIC CRUSHABLE FOAM is used to model foams which are transversely isotropic, crushable, low density, and without Poisson effects and is often used in energy-absorbing structures; MAT CLOSED CELL FOAM is used to model low density, closed cell polyurethane foams used as impact liners for automotive applications; and MAT LOW DENSITY VISCOUS FOAM is used to model low density, rate sensitive urethane foams with high compressibility used for seat cushions and padding. Additionally there are 16 other material models that can be used to model foams. However, no single general material model exists that cover a wider range of usage scenarios and loads.

2.6 Arc Length Method - Riks analysis

In situations where a loaded structure encounters an instability, where the load-displacement response shows a negative stiffness, the use of the arc-length method [21] is a suitable approach [22]. As the compressive response of the foam material contains an instability, the Arc Length Method is a suitable analysis type for the current problem.

In the arc-length method both the displacement, \mathbf{u} , and load, λ , are incremented, by $\Delta\mathbf{u}$ and $\Delta\lambda$ respectively, and both are treated as unknowns such that the equation to solve is

$$\mathbf{R}(\mathbf{u}', \lambda') = \mathbf{F}^{\text{int}}(\mathbf{u}_0 + \Delta\mathbf{u}) - (\lambda_0 + \Delta\lambda)\mathbf{q} = \mathbf{0} \quad (2.4)$$

where \mathbf{F}^{int} is the internal force vector, \mathbf{q} is the external force vector, and \mathbf{R} is the residual.

If the next incrementation of $\Delta\mathbf{u}$ and $\Delta\lambda$ is not on the equilibrium path, the solution for that incrementation step is obtained by iteration around a new point $(\mathbf{u}_0 + \Delta\mathbf{u} + \delta\mathbf{u}, \lambda_0 + \Delta\lambda + \delta\lambda)$ such that

$$\mathbf{R}(\mathbf{u}'', \lambda'') = \mathbf{F}^{\text{int}}(\mathbf{u}_0 + \Delta\mathbf{u} + \delta\mathbf{u}) - (\lambda_0 + \Delta\lambda + \delta\lambda)\mathbf{q} = \mathbf{0} \quad (2.5)$$

By using a Taylor series expansion on \mathbf{F}^{int} , and keeping the linear terms, the previous equation is rewritten as

$$[\mathbf{K}_T]_{\mathbf{u}_0 + \Delta\mathbf{u}} \delta\mathbf{u} - \delta\lambda\mathbf{q} = \mathbf{F}^{\text{int}}(\mathbf{u}_0 + \Delta\mathbf{u}) - (\lambda_0 + \Delta\lambda)\mathbf{q} = -\mathbf{R}(\mathbf{u}', \lambda') \quad (2.6)$$

where

$$[\mathbf{K}_T]_{\mathbf{u}_0+\Delta\mathbf{u}} = \left[\frac{\partial \mathbf{F}^{\text{int}}(\mathbf{u})}{\partial \mathbf{u}} \right]_{\mathbf{u}_0+\Delta\mathbf{u}} \quad (2.7)$$

As both $\delta\mathbf{u}$ and $\delta\lambda$ are unknowns one additional equation is needed. This is the Arc Length Equation

$$(\Delta\mathbf{u} + \delta\mathbf{u})^T (\Delta\mathbf{u} + \delta\mathbf{u} + \Psi^2(\Delta\lambda + \delta\lambda)^2(\mathbf{q}^T \mathbf{q})) = \Delta l^2 \quad (2.8)$$

where Ψ determines the relation between the load- and displacement increment, and Δl determines the length of the increment.

The arc-length method can then be summarised to the following equation system

$$\begin{bmatrix} \mathbf{K}_T & -\mathbf{q} \\ 2\Delta\mathbf{u}^T & 2\Psi^2\Delta\lambda(\mathbf{q}^T \mathbf{q}) \end{bmatrix} \begin{bmatrix} \delta\mathbf{u} \\ \delta\lambda \end{bmatrix} = - \begin{bmatrix} \mathbf{R} \\ A \end{bmatrix} \quad (2.9)$$

where

$$\begin{aligned} \mathbf{R} &= \mathbf{F}^{\text{int}}(\mathbf{u}_0 + \Delta\mathbf{u}) - (\lambda_0 + \Delta\lambda)\mathbf{q} \\ A &= -(\Delta\mathbf{u}^T \Delta\mathbf{u} + \Psi^2\Delta\lambda^2(\mathbf{q}^T \mathbf{q}) - \Delta l^2) \end{aligned} \quad (2.10)$$

3

Method

The aim of the project was to capture the mechanical response of a closed cell foam in compression, tension, and shear by representing the foam with a geometric structure comprised of shell elements and subjecting the structure to varying loads. A great amount of analyses were performed to find the optimal mesh, analysis type, shape and thickness of the structure, and material parameters. Due to the high number of analyses, an RVE together with PBC's was used to reduce the number of elements needed in the FE model, and thereby the analysis time.

To anchor the chosen geometric shape to the physical structure of foam, as well as to get an initial guess for further optimisation, a microstructure study of the size and elongation of the foam cells was performed. With the input from the microstructure study, as well as from the literature survey, the material parameters and geometric parameters were optimised for H100 with the software LS-OPT.

After optimisation of parameters for H100 the results from the microstructure study was used to re-scale the geometry to H60. An analysis was then run with the same material parameters as for H100 to validate the material parameters found in the optimisation procedure.

3.1 FEM implementation of RVE

The basis of the FE modelling was to use an RVE to capture the macroscale material behaviour. RVE's are commonly used to simulate large systems where the structure is periodic and can be properly represented by repeating a single RVE. Together with the implementation of PBC's, the correct material response can be captured with a drastically reduced analysis time. [23]

3.1.1 Periodic Boundary Conditions

PBC's are used to emulate that the RVE is connected to an equal RVE on the boundary where the PBC is applied. PBC's can hence be applied on all six boundaries to capture the material response of an infinitely large piece of material. The PBC is implemented by connecting the nodes on the faces, edges, and vertices and constricting them to behave equal to the nodes on the opposite side by enforcing equations between them. In displacement controlled analyses a deformation is added to the equations such that the desired global strain is achieved. The faces, edges, and vertices on a cubical RVE are identified in Figure 3.1.

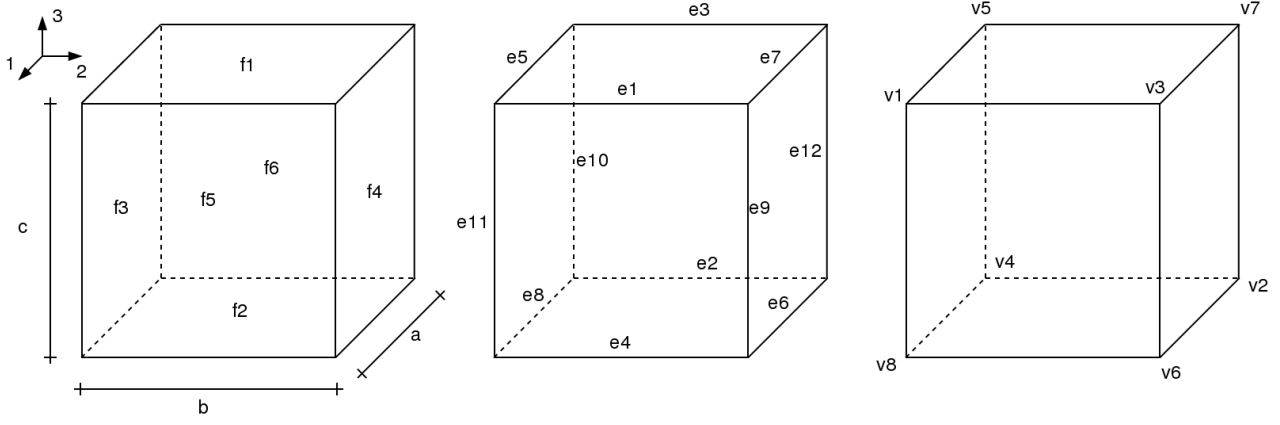


Figure 3.1: Faces (f), edges (e), and vertices (v) of a cubical RVE

When applying PBC's on the faces, the nodes on opposing faces are connected to each other resulting in three sets of equations, one set for each pair of faces. All six Degrees of Freedom (DoF), i , are restricted resulting in equations for translations as well as rotations. The applied deformation is added to the equations by adding a contribution in translation or rotation to the equilibrium according to

$$\begin{aligned}
 u_i^{f1} - u_i^{f2} - c\epsilon_{3i}^0 &= 0 \\
 u_i^{f3} - u_i^{f4} + b\epsilon_{2i}^0 &= 0 \\
 u_i^{f5} - u_i^{f6} - a\epsilon_{1i}^0 &= 0
 \end{aligned} \tag{3.1}$$

where u_i^{f1} is the translation in the DoF i for the set of nodes located on face f1, a , b , and c are the initial distances between the faces along the 1-, 2-, and, 3-axes respectively, and ϵ_{1i}^0 , ϵ_{2i}^0 , and ϵ_{3i}^0 are the desired global strains. The global strains do not contain rotations, so for $i > 3$ these are simply set to zero efficiently constraining rotations as well as translations.

To implement the PBC's on the edges, three master edges are defined, and each master edge is connected to three slave edges. This results in nine sets of equations. In the following equations, edges 1, 5, and 9 are used as master edges.

$$\begin{aligned}
 u_i^{e1} - u_i^{e2} - a\epsilon_{1i}^0 - c\epsilon_{3i}^0 &= 0 \\
 u_i^{e1} - u_i^{e3} - a\epsilon_{1i}^0 &= 0 \\
 u_i^{e1} - u_i^{e4} - c\epsilon_{3i}^0 &= 0 \\
 u_i^{e5} - u_i^{e6} + b\epsilon_{2i}^0 - c\epsilon_{3i}^0 &= 0 \\
 u_i^{e5} - u_i^{e7} + b\epsilon_{2i}^0 &= 0 \\
 u_i^{e5} - u_i^{e8} - c\epsilon_{3i}^0 &= 0 \\
 u_i^{e9} - u_i^{e10} - a\epsilon_{1i}^0 - b\epsilon_{2i}^0 &= 0 \\
 u_i^{e9} - u_i^{e11} - b\epsilon_{2i}^0 &= 0 \\
 u_i^{e9} - u_i^{e12} - a\epsilon_{1i}^0 &= 0
 \end{aligned} \tag{3.2}$$

For the vertices two master vertices are defined, where the first master vertex, v1, is connected to three slave vertices, and the second master vertex, v3, is connected to four slave vertices. In these last

connection the first master vertex is included as a slave, resulting in seven equations.

$$\begin{aligned}
 u_i^{v1} - u_i^{v8} - c\epsilon_{3i}^0 &= 0 \\
 u_i^{v1} - u_i^{v2} - a\epsilon_{1i}^0 + b\epsilon_{2i}^0 - c\epsilon_{3i}^0 &= 0 \\
 u_i^{v1} - u_i^{v7} - a\epsilon_{1i}^0 + b\epsilon_{2i}^0 &= 0 \\
 u_i^{v3} - u_i^{v6} - c\epsilon_{3i}^0 &= 0 \\
 u_i^{v3} - u_i^{v4} - a\epsilon_{1i}^0 - b\epsilon_{2i}^0 - c\epsilon_{3i}^0 &= 0 \\
 u_i^{v3} - u_i^{v5} - a\epsilon_{1i}^0 - b\epsilon_{2i}^0 &= 0 \\
 u_i^{v3} - u_i^{v1} - b\epsilon_{2i}^0 &= 0
 \end{aligned} \tag{3.3}$$

3.1.2 PBC implementation in Abaqus

The PBC's were implemented in Abaqus by using the *EQUATION command. This command creates a linear constraint equation consisting of N terms on the form $A_1 u_i^P + A_2 u_j^Q + \dots + A_N u_k^R = 0$ where A_N is a constant and u_i^P is a nodal variable at node P with DoF i . The corresponding commands for the Abaqus input file can be seen in Listing 3.1.

Listing 3.1: General *EQUATION definition in Abaqus input file

```
*EQUATION
N
P, i, A1, Q, j, A2, ... R, k, AN
```

Therefore, to specify that the two nodes P and Q are to have equal displacement in the x -direction, i.e. $u_1^P - u_1^Q = 0$, the equation in the Abaqus input file is written as Listing 3.2.

Listing 3.2: *EQUATION definition in Abaqus input file to specify equal displacement

```
*EQUATION
2
P, 1, 1, Q, 1, -1
```

However, if it is desired that two nodes should displace a specified distance in relation to each other, i.e. $A_1 u_i^P + A_2 u_j^Q + \dots + A_N u_k^R = \hat{u}$, a “dummy node” has to be introduced. The equation is then rewritten as $A_1 u_i^P + A_2 u_j^Q + \dots + A_N u_k^R - \hat{u}_m^Z = 0$ where Z is the dummy node and \hat{u}_m the prescribed displacement in the m :th DoF. Therefore, to specify that the two nodes P and Q are to decrease the distance between them by \hat{u} in the x -direction, i.e. $u_1^P - u_1^Q = \hat{u}_1^Z$, the Abaqus command is written as Listing 3.3.

Listing 3.3: *EQUATION definition in Abaqus input file to specify displacement of nodes

```
*EQUATION
3
P, 1, 1, Q, 1, -1, Z, 1, -1
```

The nodes that are to be linearly constrained were gathered using a Matlab script¹, see Appendix A.1, which also writes the relevant Abaqus commands to a .inp file. When specifying the constraints to the edges (and vertices) it is important to always write the slave nodes first, as these nodes will be eliminated to impose the constraints. The implementation of dummy nodes in Abaqus introduced three additional nodes. These nodes, \hat{u}_i^1 , \hat{u}_i^2 , and \hat{u}_i^3 , control the relative displacements for one pair of sides each and were thus used to impose the strains ϵ_{1i}^0 , ϵ_{2i}^0 , and ϵ_{3i}^0 respectively.

¹The naming of edges and faces in the Matlab script do not coincide with the convention used in Section 3.1.1

3.1.3 Verification of the PBC's

To confirm that the PBC's work, tests were carried out on a cubic RVE test piece, laminated with four layers of material with different stiffness. A strain was applied in the 3-direction on the top and bottom face and the other sides were constrained in their normal directions inducing macroscopic uniaxial strain. When applying a certain strain, the RVE showed a repetitive deformation in all points on all faces. Smaller RVE's from the test piece were then isolated and the same strain was applied as on the larger RVE to certify that the same stresses and strains would occur in each of the smaller RVE's as on the larger RVE. The PBC's were found to work for an applied normal strain as well as shear strain.

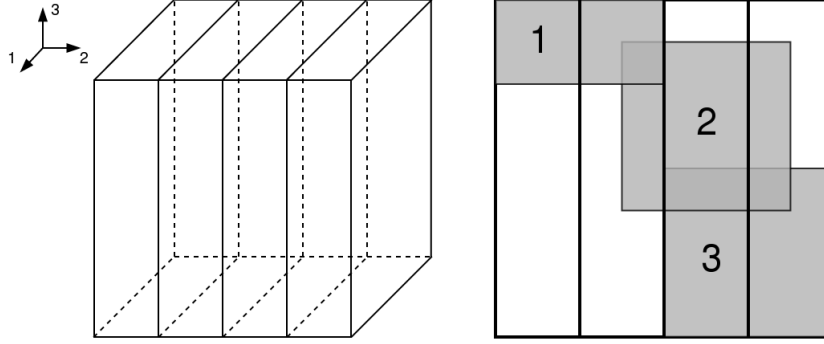


Figure 3.2: The laminate test cube with RVE's 1, 2, and 3

The PBC's were verified under uniaxial strain condition. Later analyses also introduced uniaxial stress, where the implementation of the PBC's is identical, but the execution differs slightly. These were not verified on the test setup described.

3.2 Analysis setup

In the setup of the FE analyses a geometry representing the foam was chosen and appropriate boundary conditions were imposed implementing the periodicity of the RVE and introducing the applied strain to the geometry. The types of analyses used to run and verify the simulations were determined with regards to accuracy and efficiency. To initiate buckling, an imperfection obtained from a buckling analysis was added to the geometry.

3.2.1 Geometry and Material

The Kelvin tetrakaidecahedron was chosen to represent the foam microstructure in the current project. It was chosen over the Weaire-Phelan model due to the small differences in mechanical response between them and due to its lesser complexity. PBC's were confirmed to work also for the Kelvin model² and therefore only a single RVE was used for the subsequent analyses.

The Kelvin geometry was created using the software Surface Evolver [24]. In the software, an RVE was exported as a .stl file and imported into ANSA [25] for meshing. This RVE consists of eight hexagonal faces, six quadrilateral faces, and 12 triangular faces, see Figure 2.5b. When the RVE is duplicated and repeated in all directions, four triangular faces will make up one quadrilateral face. Note that opposing quadrilateral faces do not exist to avoid duplicate thicknesses when the RVE is repeated. A nodal mapping was implemented such that the cell could be elongated in any direction by a chosen scaling factor to implement the transverse isotropy observed in the foam. The resulting mean minor diameter from the microstructure study of H60 and H100 was chosen as the minor diameter of the RVE for H60 and H100 respectively. Although the absolute dimensions of the RVE do not influence the results of the performed analyses, as first order homogenisation is used, having appropriate dimensions results

²Note that the Kelvin geometry does not include vertices

in a derived cell wall thickness that is comparable to the physical cell wall thickness. The material was defined as isotropic elastoplastic, utilising isotropic hardening for the plastic behaviour.

3.2.2 Boundary conditions and loads

With the implementation of the PBC's, the nodes on all sides of the RVE were connected to their respective dummy nodes \hat{u}^i , where $i = 1, 2, 3$ denotes the normal direction for the respective sides. Therefore, macroscopic uniaxial stress or strain could be imposed on the RVE by controlling the displacements of the dummy nodes. Six types of analyses were conducted on the RVE under both macroscopic uniaxial strain and uniaxial stress conditions; tension in the 1- and 3-direction, compression in the 1- and 3-direction, and shear in the 12- and 32-direction.

The applied boundary conditions prescribed to the RVE to achieve macroscopic uniaxial strain and uniaxial stress are summarised in Equation 3.4 and 3.5 respectively.³ The nonzero prescribed displacements were applied as linearly increasing over the analyses.

Uniaxial strain:

$$\begin{aligned}
 \text{Tension in the 1-dir: } & \hat{u}_1^1 = a\epsilon_{11}^0, & \hat{u}_m^2 = \hat{u}_m^3 = 0 \quad \forall m, & u_k^D = 0 \\
 \text{Tension in the 3-dir: } & \hat{u}_3^3 = c\epsilon_{33}^0, & \hat{u}_m^1 = \hat{u}_m^2 = 0 \quad \forall m, & u_k^D = 0 \\
 \text{Compression in the 1-dir: } & \hat{u}_1^1 = a\epsilon_{11}^0, & \hat{u}_m^2 = \hat{u}_m^3 = 0 \quad \forall m, & u_k^D = 0 \\
 \text{Compression in the 3-dir: } & \hat{u}_3^3 = c\epsilon_{33}^0, & \hat{u}_m^1 = \hat{u}_m^2 = 0 \quad \forall m, & u_k^D = 0 \\
 \text{Shear in the 12-dir: } & \hat{u}_2^1 = a\gamma_{12}^0, \quad \hat{u}_1^1 = 0, & \hat{u}_m^2 = \hat{u}_m^3 = 0 \quad \forall m, & u_k^D = 0 \\
 \text{Shear in the 32-dir: } & \hat{u}_2^3 = c\gamma_{32}^0, \quad \hat{u}_3^3 = 0, & \hat{u}_m^2 = \hat{u}_m^1 = 0 \quad \forall m, & u_k^D = 0
 \end{aligned} \tag{3.4}$$

Uniaxial stress:

$$\begin{aligned}
 \text{Tension in the 1-dir: } & \hat{u}_1^1 = a\epsilon_{11}^0, & u_k^D &= 0 \\
 \text{Tension in the 3-dir: } & \hat{u}_3^3 = c\epsilon_{33}^0, & u_k^D &= 0 \\
 \text{Compression in the 1-dir: } & \hat{u}_1^1 = a\epsilon_{11}^0, & u_k^D &= 0 \\
 \text{Compression in the 3-dir: } & \hat{u}_3^3 = c\epsilon_{33}^0, & u_k^D &= 0 \\
 \text{Shear in the 12-dir: } & \hat{u}_2^1 = a\gamma_{12}^0, & \hat{u}_1^1 = \hat{u}_1^2 = \hat{u}_3^2 = \hat{u}_1^3 = \hat{u}_2^3 = 0, & u_k^D = 0 \\
 \text{Shear in the 32-dir: } & \hat{u}_2^3 = c\gamma_{32}^0, & \hat{u}_3^3 = \hat{u}_1^2 = \hat{u}_3^2 = \hat{u}_2^1 = \hat{u}_3^1 = 0, & u_k^D = 0
 \end{aligned} \tag{3.5}$$

where \hat{u}_m^i is the displacement for dummy node i in the m :th DoF, $\epsilon_{i,m}^0$ is the desired global strain for dummy node i in the m :th DoF, and u_k^D is the displacements for a node D in directions $k = 1, 2, 3$ which acts as a Dirichlet boundary condition.

One disadvantage with using an RVE with PBC's applied to it is that the progressive crushing can not be captured. The progressive crushing is caused by local buckling of cells layer by layer, as can be seen in studies done by, e.g., Tita et al. [26]. Fundamental to the theory of PBC's are that all surrounding RVE's behave identically, implying that all cells will buckle simultaneously. The current technique could hence only capture the elastic regime and the initial global buckling of the foam. Therefore, the compression analyses are run to 5% global strain, where the global buckling is presumed to be completed. In tension, FEA analyses are run until fracture occurs in the experimental results. The final strain for the shear analyses was chosen as the point where the experimental results levels out at 10% for both the 1- and 3-direction.

³The boundary conditions for the shear analyses in uniaxial strain were not implemented correctly. However, this was discovered too late in the project to rectify. This is discussed further in Section 5.5.3.

3.2.3 Analysis

Several different analysis types were investigated during the project. Due to the unstable behaviour of the buckling problem, the modified Riks analysis was deemed appropriate to properly capture the stress-strain behaviour. However, due to the long solution times of this analysis it was not suited for optimisation procedures. Instead, Dynamic Implicit was chosen with the additional option of Quasi-Static enabled. This proved to be a much more efficient solver for the problem at hand. Furthermore, the NLGEOM flag was turned on for all analyses due to the large deformations. Because of the large instability at the point of buckling, a small amount of Rayleigh damping, equal to 0.1% of the stiffness matrix, was added to the Dynamic Implicit analyses to stabilise the solution. The Riks analysis was then used to verify the dynamic analyses. For the Riks analysis, no material damping was added; however, additional constraints were used to prevent rigid body motions. An example input file for a Dynamic Implicit analysis can be seen in Appendix A.3. Please note that the parameter used for the hardening modulus in the input file is different from the material parameter hardening modulus due to the implementation of plasticity.

As the dummy nodes are connected to all prescribed nodes on their respective sides, the global engineering stress and strain of the model can be obtained by using the reaction force and displacement of the dummy nodes as

$$\sigma_{im} = \frac{F_m^i}{A_0}, \quad e_{im} = \frac{l^i - l_0^i}{l_0^i} = \frac{\hat{u}_m^i}{l_0^i} \quad (3.6)$$

where F_m^i is the reaction force for dummy node i in the m :th direction, A_0 is the initial area normal to the applied strain, e is the engineering strain, l_0^i and l^i is the respective initial and current length of the RVE in the direction of DoF i , and \hat{u}_m^i is the displacement of dummy node i in the m :th DoF.

The shear response was calculated as

$$\tau_{im} = \frac{F_m^i}{A_0}, \quad \gamma_{im} = \frac{l^i - l_0^i}{h} = \frac{\hat{u}_m^i}{h} \quad (3.7)$$

where τ is the shear stress, γ the shear angle and h is the height of the RVE normal to the face that the strain is applied to. Note that the height do not change since simple shear is applied. For example the shear stresses and strains τ_{12} and γ_{12} can be calculated as

$$\tau_{12} = \frac{F_2^1}{bc}, \quad \gamma_{12} = \frac{\hat{u}_2^1}{b} \quad (3.8)$$

3.2.4 Buckling initiation

To initiate the buckling behaviour of the cell, an imperfection was added using the Abaqus keyword *IMPERFECTION. The chosen imperfection was the complete deformation from the first buckling mode, see Figure 3.3, where the hexagonal faces alternate between deforming inwards and outwards. It was applied such that the added displacements from the buckling mode would equal between 5% and 30% of the shell thickness. Some experimentation was needed to arrive at an appropriate amount of imperfection, as with too little imperfection the buckling would not be properly initiated and with too much the buckling response would be less pronounced. This is discussed further in Section 5.5.2.

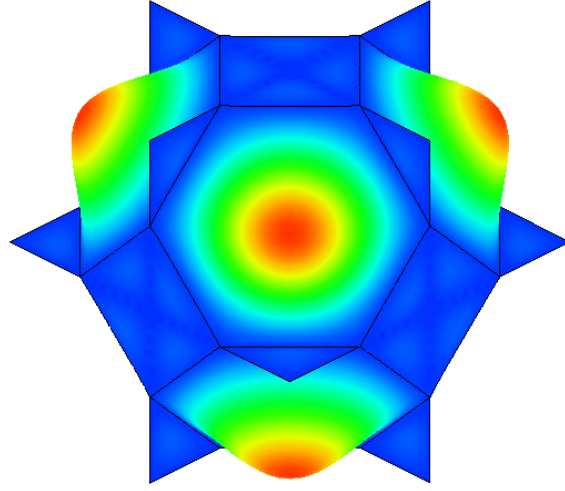


Figure 3.3: The first buckling mode

3.3 Meshing of Geometry

The geometry was meshed using shell elements, either triangular (Abaqus S3 or S3R) or quadrilateral (Abaqus S4 or S4R), where the reduced integration (R) elements were used for the final results. Five Gaussian integration points were used through the thickness of the elements. A mesh convergence study was performed to find the optimal mesh. Three different mesh structures were analysed. The first consisted only of triangular elements and is referred to as the “Triangular” mesh as seen in Figure 3.4a. The second and third meshes consisted only of quadrilateral elements with different mesh structures referred to as “Quads star”, Figure 3.4b, and “Quads straight”, Figure 3.4c. The names refer to the respective patterns on the hexagonal face of the mesh. The mesh convergence study was performed on the maximum force during a 20% strain static compression analysis in the 3-direction. During these analyses the PBC’s were executed to impose macroscopic uniaxial strain. The meshes were constructed such that the number of elements varied between approximately 500 to 15000 elements.

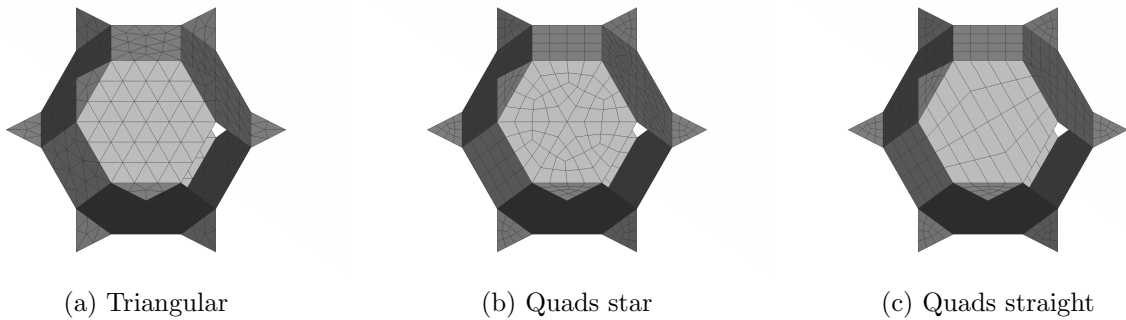


Figure 3.4: Different mesh structures

From the mesh convergence study it can be observed that the triangular mesh generally displays a stiffer response and therefore a higher reaction force compared to the quadrilateral meshes with comparable number of elements, see Figure 3.5a. Furthermore, the “Quads straight” mesh generally suffered from more convergence issues and had a worse aspect ratio in the elements. Therefore, a mesh of 6912 elements with the “Quads star” structure, see Figure 3.6, was chosen to be used throughout the rest of the project. This mesh had a relative error of approximately 1.3%, see Figure 3.5b.

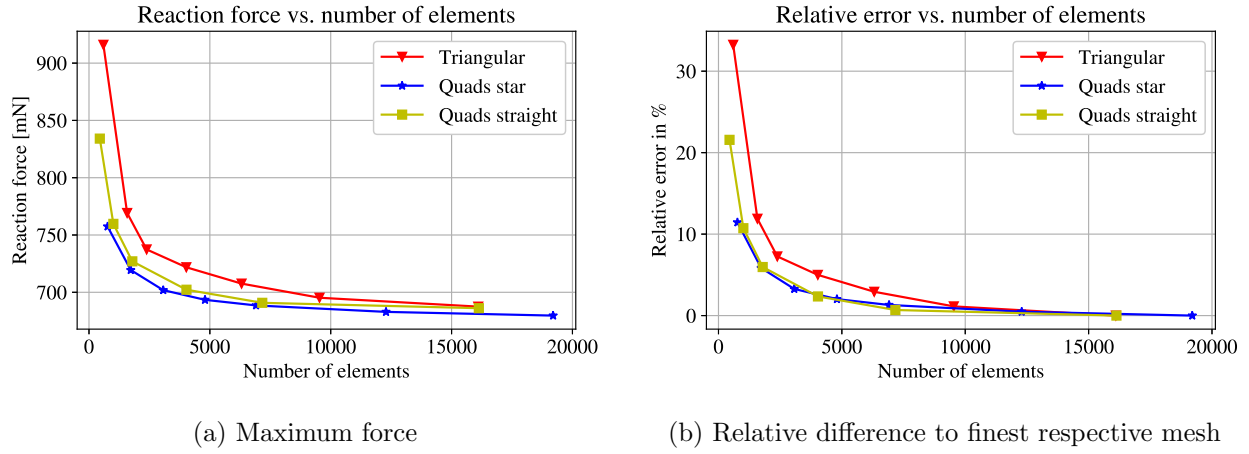


Figure 3.5: Mesh convergence study

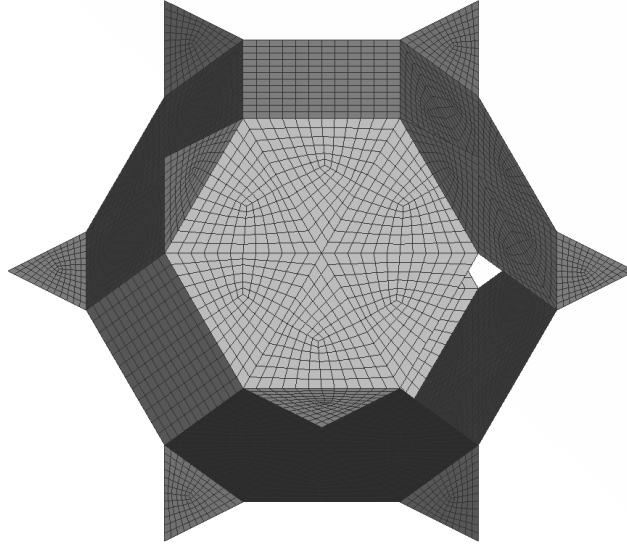


Figure 3.6: The chosen mesh with 6912 quadrilateral elements

3.4 Foam microstructure study

A study of the microstructure was conducted at Chalmers University of Technology using a Philips XL30 ESEM. A hypothesis proposed early in the project was that the size of the cells might vary in the rise direction of the foam. The aim of the study was hence to investigate the shape and dimensions of the cells and their variations in the rise direction. This was done by taking images of the cells in the 1-3 plane in layers at different heights of the foam. With good results, this would bring clarity to the physical shape of the cells such that a suitable approximation could be made for the FE modelling.

Foam samples were provided by Diab and prepared for the ESEM by the project participants. Images of the specimens were captured in the microscope and analysed using the software ImageJ to extract the desired data. The study was conducted on Divinycell H60 and H100.

A comparison between all layers through the thickness could only be conducted on Divinycell H100 since no maximum thickness sheet was available for H60. This thinner sheet of foam does not contain the entire thickness of the original block making a complete comparison in the rise direction of the material unattainable.

3.4.1 Specimen preparation

Test rods were cut from five different layers in the rise direction for H100, and three layers for H60, see Figure 3.7. To get as clean cut surfaces as possible the rods were notched, submerged in liquid nitrogen for approximately two minutes, then broken along the notch to produce good surfaces for the microstructure study. The rods were then cut to size and fastened on ESEM specimen mounts and sputtered with gold for 30 seconds in an Edwards Sputter Coater S150B to become conductive.

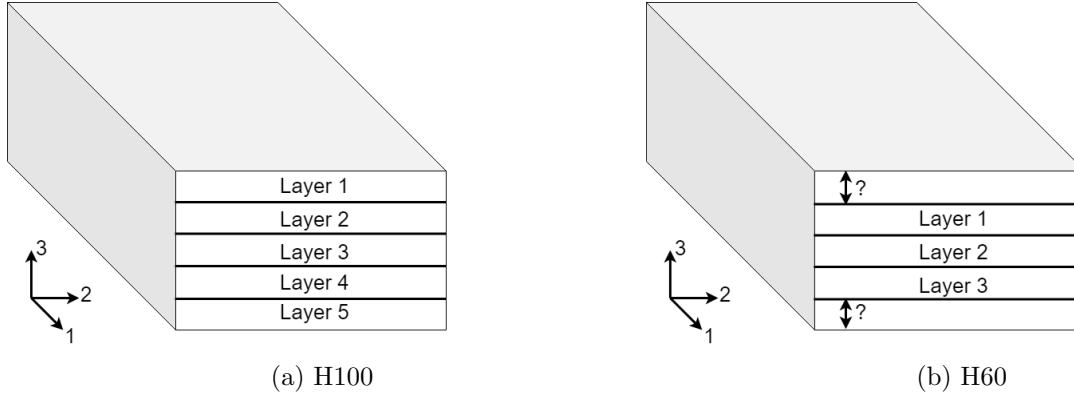


Figure 3.7: Layer selection

3.4.2 Image retrieval

Since the investigated foams are non conductive, the Gaseous Secondary Electron Detector (GSED) was used to capture images of the foam. In this technique the working gas in the specimen chamber is water vapour. When the electron beam is directed towards the specimen the secondary electrons in the water is lost to the specimen, giving it a negative charge⁴ that is captured by the GSED.

The amount of cells identified by ImageJ in each layer is summarised in Table 3.1. Two images were captured per layer for H60 and three per layer for H100.

Table 3.1: Number of cells identified by ImageJ in ESEM images

Foam	Layer 1	Layer 2	Layer 3	Layer 4	Layer 5	Total amount
H60	252	276	303	N/A	N/A	831
H100	249	335	343	368	277	1572

3.4.3 Image analysis

The images were analysed using the software ImageJ [27] and the plugin MorphoLibJ [28]. They were made binary using the Auto Local Threshold feature in ImageJ and further processed using the Watershed Segmentation algorithm in MorphoLibJ to extract the cell outlines. With binary images clearly showing the cell outlines, the cells were analysed using the Analyze Particles function in ImageJ. As the goal of the study was to measure the cell size and elongation, ellipses were fitted to the cells and the major and minor axis measured. Example images showing the results from ImageJ can be seen in Figure 3.8, and the complete collection of images can be found in Appendix A.4.

⁴In order for the specimen to pick up the secondary electrons large areas of complete non conductivity must be avoided. Gold sputtering was therefore used to enhance the quality of the images.

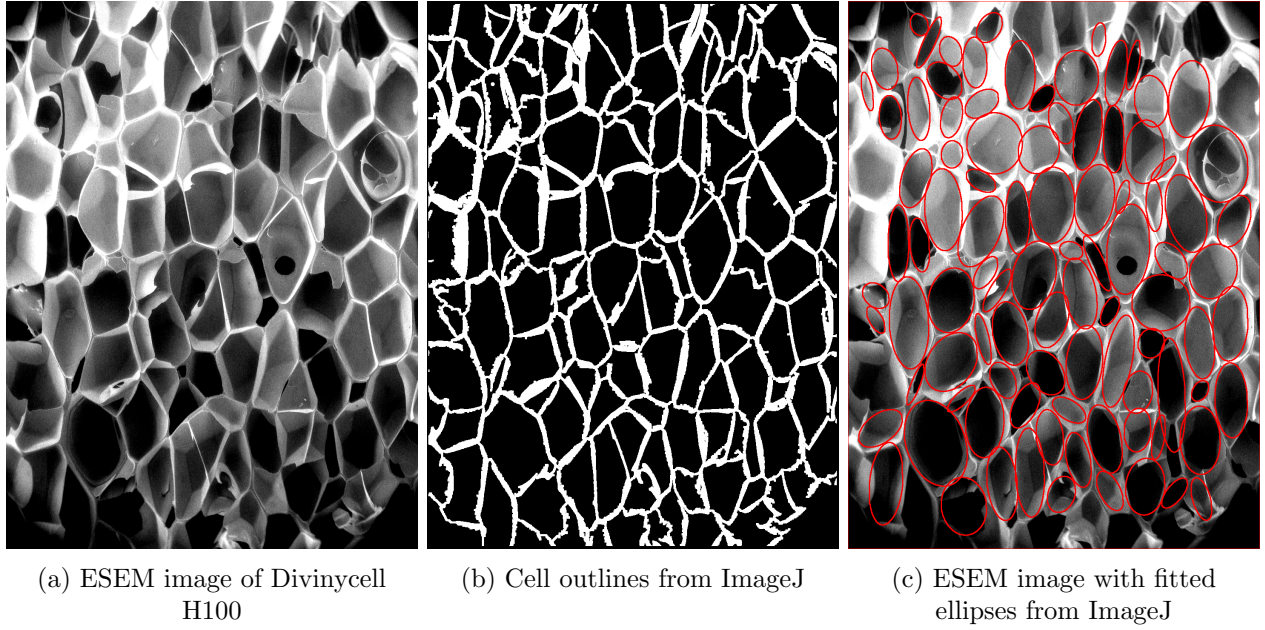


Figure 3.8: Image analysis

3.5 Parameter optimisation using LS-OPT

The mechanical response of the foam model is governed by a variety of parameters, making a structured procedure necessary when optimising the parameters. The bulk material parameters chosen for the optimisation procedure were Young's modulus (E_s), yield stress (Y_s), and isotropic hardening modulus (H_s), and the geometric parameters chosen were cell wall thickness (t) and cell elongation (L). Since several of these parameters, e.g. Young's modulus and cell wall thickness, have strong correlations the designated optimisation software LS-OPT [29] was used to automate the optimisation. LS-OPT is a design optimisation and analysis tool which uses predefined algorithms to find the optimal values for user defined parameters by attempting to match, e.g., FEA results to experimental data.

The calibration of material and geometric parameters was carried out on H100 in compression and tension in the 1- and 3-directions. With a good correlation between experimental and FE data, the parameters were manually verified with shear analyses. If the results from the shear analyses were a good match towards the experimental data, the calibration could be deemed successful independent of loading scenario.

No optimisation of parameters were conducted for H60. Instead, the material parameters from the H100 optimisation were kept, while the geometric parameters were re-scaled to fit the H60 geometry according to the ESEM study, further explained in Section 3.6. With a good correlation between experimental and FE data for H60, the material parameters derived in the optimisation procedure can be deemed correct.

To set up the optimisation software, the minimum, maximum, and starting values for the optimisation parameters need to be determined. For the bulk material parameters these values are hard to estimate since the behaviour of the material when solidified into a foam differs from that of the same material solidified into a solid rod. Therefore, these parameters can not simply be extracted from tensile tests on a test coupon. The range of values for the parameters E_s , Y_s , and H_s were therefore based on the parameters of standard PVC material [30]. The cell walls in the current study were estimated to have a uniform thickness, i.e. no Plateau borders were implemented. This equivalent uniform thickness was calculated as

$$t = \frac{V\rho^*}{A\rho_s} \quad (3.9)$$

where V is the volume of the bounding box of the RVE and A is the surface area of all surfaces in the RVE. This calculated thickness was used to determine a suitable range of values for the optimisation procedure. Finally, the minimum, maximum, and starting values for the cell elongation were determined based on the ESEM study and other relevant literature [2].

3.5.1 LS-OPT setup

The LS-OPT configuration is comprised of three main steps; the initial Setup of the optimisation, the Sampling and Analysis stages, and the Optimization procedure, see Figure 3.9.

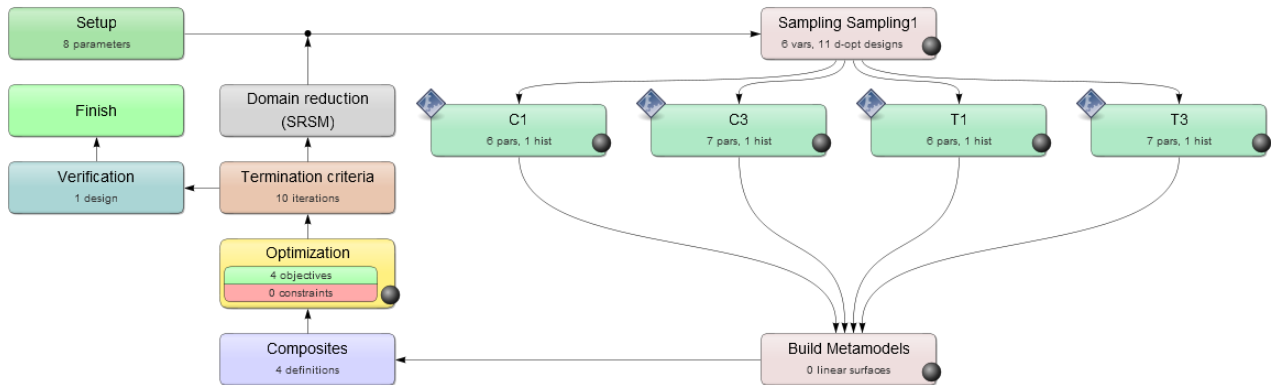


Figure 3.9: LS-OPT main screen

In the Setup step, the parameters that are to be used in the optimisation procedure are defined as a range of values, a fixed value, or as a function of other variables. The same parameters are introduced into the .inp files by using the Abaqus keyword *PARAMETER, see Listing 3.4. The parameters enclosed with double angle brackets are then replaced by the values specified in the Setup stage before the analyses are run in the Sampling and Analysis stage.

Listing 3.4: .inp file with parameter definitions for LS-OPT

```

*PARAMETER
t = <<t>>
E = <<E>>
Y = <<Y>>
H = <<H>>

```

Several .inp files are created with varying parameters for each iteration for the specified analyses; compression and tension in the 1- and 3-directions (C1, C3, T1, T3⁵). The analyses with inserted parameters are run by using .bat files, see Listing 3.5. In these files, executed by LS-OPT, Abaqus is called with the created .inp file as an input. After the analyses have been completed the relevant results needed for the next step is extracted using a Python script, see Appendix A.2. When all the analyses for an iteration have been completed, the Optimization step starts.

Listing 3.5: Example of a .bat file used by LS-OPT to run analyses

```

@echo off
set abqexe=abq2018
set job=inputfile
:: -----
COPY bucklefile.fil
:: Execute abaqus and wait for completion
call %abqexe% interactive job=%job% cpus=8

```

```

:: Check if recent analysis has completed successfully
findstr /I /c:"THE ANALYSIS HAS COMPLETED SUCCESSFULLY" %job%.sta >nul
set RESULT=%ERRORLEVEL%
if %ERRORLEVEL%==0 (
    echo.
    echo 'N o r m a l'
    echo.
) else (
    echo.
    echo 'E r r o r'
    echo.
)
:: Run python script to extract results
%abqexe% python results_extraction.py

```

With results for a wide range of values for the chosen parameters, the results are matched towards the experimental data and the root-mean-square (RMS) of the error between FE-data and experimental data is calculated. Based on the RMS values for the analyses with varying parameters, LS-OPT uses algorithms⁶ to suggest new values which should provide better RMS values. This process of running several analyses with different parameters for each iteration is continued until the specified maximum number of iterations is reached or the combined results are within a given tolerance.

3.6 Re-scaling of geometric parameters to the H60 foam

Since the cells are not perfectly arranged in the rise direction of the foam the value of cell elongation from the ESEM study was assumed to be incorrect. However, since the microstructure study was conducted identically for H60 as for H100 the relative difference in cell elongation was assumed to be correct. Therefore, the geometric parameters optimised for H100 could be used, together with the results from the microstructure study, to derive the appropriate geometric parameters for H60.

The elongation of H60 to be used in the FE model, $L_{FE,H60}$, can be derived from the optimised elongation of H100 and the results from the microstructure study using the following relation

$$\frac{L_{FE,H100}}{L_{ESEM,H100}} = \frac{L_{FE,H60}}{L_{ESEM,H60}} \quad (3.10)$$

where $L_{FE,H100}$ denotes the optimised value of elongation for H100, as used in the FE-analyses, and $L_{ESEM,H100}$ and $L_{ESEM,H60}$ denotes the elongations found in the microstructure study.

The thickness of a cell wall can theoretically be calculated as in Equation (3.9). Since this equation uses the approximation that the cell walls are of a constant thickness, which is an incorrect approximation, this value was also optimised for in the analysis of H100. Known constants after optimisation are the surface area of a cell, the volume of the RVE, the density of the bulk material, and the cell wall thickness. The macroscale density of the H100 foam, which previously was assumed known as 100 kg/m³ in Equation (3.9), is re-calculated as

$$\rho_{H100}^* = \frac{t_{H100} A_{H100} \rho_S}{V_{H100}} \quad (3.11)$$

Since the macroscale density of H60 ideally is 60% of H100, the equivalent optimised wall thickness of H60 is calculated as

$$t_{H60} = \frac{V_{H60} \rho_{H100}^* 0.6}{A_{H60} \rho_S} \quad (3.12)$$

⁵For tension in the 3-direction the analyses were performed to only 2% global strain as this analysis was very hard to match to the experimental data and it was not favourable to let this analysis to overly influence the parameters.

⁶LS-OPT used Adaptive Simulated Annealing (ASA) to find a global optimum, and then switched to Leapfrog Optimisation (LFOP) to find a local optimum if a global optimum was achieved.

3.7 Calculation of global material parameters

After the FE analyses have been completed, the global material parameters can be calculated and compared to the experimental parameters.

The global Elastic modulus in the i -direction is calculated from the tension analysis in the i -direction as

$$E_{ii}^* = \frac{\Delta \sigma_{ii}}{\Delta \epsilon_{ii}} \quad (3.13)$$

where Δ denotes the elastic region and σ_{ij} and ϵ_{ij} is the stress and strain in the ij -direction.

The global shear modulus is calculated in a similar manner as

$$G_{ij}^* = \frac{\Delta \tau_{ij}}{\Delta \gamma_{ij}} \quad (3.14)$$

where γ_{ij} is the shear angle in the ij -direction

The global Poisson's ratio is calculated from tension analyses in the i -direction as

$$\nu_{ij}^* = \frac{\epsilon_{jj}}{\epsilon_{ii}} \quad (3.15)$$

where ϵ_{kk} is the strain in the kk -direction in the elastic region.

4

Results

In this section the results of the project are presented. Stress-strain results for H100 under both uniaxial strain and stress conditions, gathered by optimising geometric- and material parameters, are shown together with colour plots of the loaded geometry. The resulting geometric parameters from this optimisation procedure was then re-scaled to fit H60, using the information from the ESEM study, while the material parameters were kept the same. The resulting stress-strain curves and colour plots for H60 shown in this section was therefore achieved without any optimisation for that specific foam density. Furthermore, some error sources are evaluated to determine their influence on the final results.

4.1 ESEM study

The results from the ESEM study are visualised using box plots, see Figures 4.1 and 4.2. In the figures the data from each layer is presented individually as well as in a combined data set. By using box plots, the first, second, third, and fourth quartiles are shown as well as the median (orange line), mean (green triangle), and outliers (black circles) which provides an overview of the obtained data. It is clear that the dimensions and geometry of individual cells vary to a great extent in the layers, and that the general dimensions vary between layers. However, no clear pattern was found for the variations. Due to the method in which the data was obtained, namely by looking at cross sections of several specimens, it cannot be known if an observed cell was cut in the middle, which would show the correct size, or cut in a different plane which would show a smaller outline than the actual cell size. Furthermore, it can not be known if the observed cells lie in the plane orthogonal to the observation axis which adds an additional degree of uncertainty to the observed sizes and elongations.

As the major diameter observed is always less than or equal to the correct major diameter, the data collected should underestimate the actual major diameter which explains the large amount of outliers above the box plot. For the minor diameter, both smaller and larger values than the correct minor diameter can be observed.

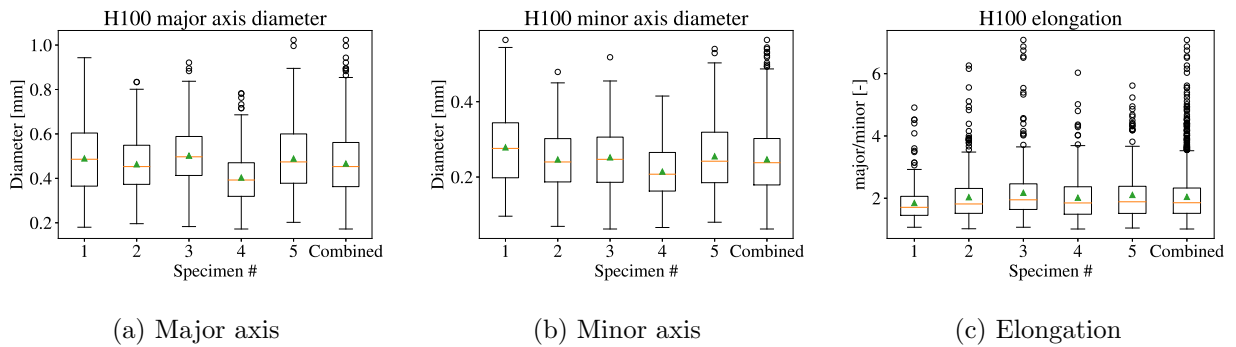


Figure 4.1: Box plots for H100 foam cell dimensions where the orange line denotes the median and the green triangle denotes the mean

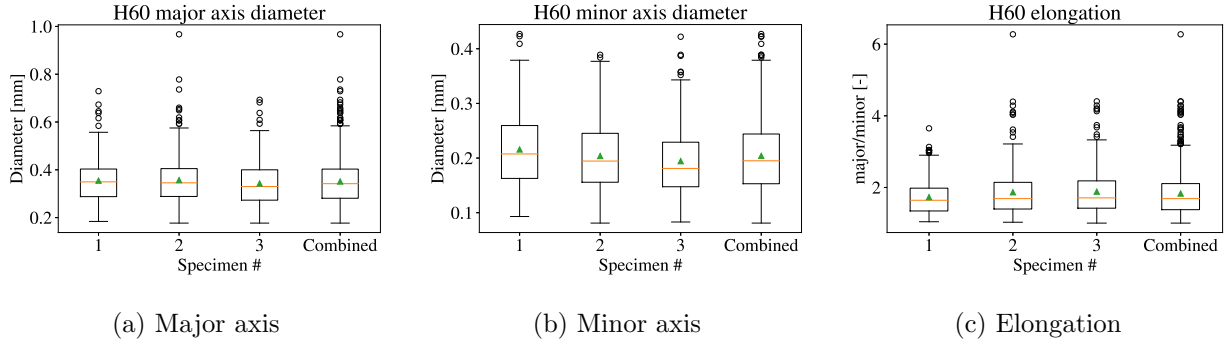


Figure 4.2: Box plots for H60 foam cell dimensions where the orange line denotes the median and the green triangle denotes the mean

The data seen in Figure 4.1 and 4.2 is summarised in Tables 4.1 and 4.2.

Table 4.1: Extracted geometrical data for Divinycell H100

	Major mean [mm]	Major me- dian [mm]	Minor mean [mm]	Minor me- dian [mm]	Elong. mean [-]	Elong. me- dian [-]
# 1	0.4897	0.4860	0.2787	0.2760	1.8479	1.7089
# 2	0.4633	0.4530	0.2466	0.2400	2.0332	1.8166
# 3	0.5022	0.4970	0.2522	0.2470	2.1760	1.9498
# 4	0.4036	0.3925	0.2144	0.2075	2.0181	1.8491
# 5	0.4890	0.4740	0.2550	0.2420	2.1063	1.8864
Comb.	0.4665	0.4530	0.2469	0.2380	2.0444	1.8556

Table 4.2: Extracted geometrical data for Divinycell H60

	Major mean [mm]	Major me- dian [mm]	Minor mean [mm]	Minor me- dian [mm]	Elong. mean [-]	Elong. me- dian [-]
# 1	0.3548	0.3495	0.2158	0.2075	1.7296	1.6428
# 2	0.3569	0.3455	0.2038	0.1945	1.8668	1.6893
# 3	0.3430	0.3300	0.1943	0.1810	1.8846	1.7091
Comb.	0.3512	0.3420	0.2040	0.1950	1.8320	1.6890

4.2 Optimisation of mechanical behaviour

After optimisation in tension and compression for H100, with the two different boundary conditions, the material parameters in Table 4.3 were obtained. The material parameters from H100 uniaxial stress were then kept for H60 and the cell wall thickness, t , and cell elongation, L , were re-scaled. The parameters in Table 4.3 were used to produce all the results found in the subsequent sections.

Table 4.3: Final parameters for the analyses

Analysis	E_s [GPa]	Y_s [MPa]	H_s [MPa]	t [μm]	L [-]
H100 uniaxial strain	2.07	37.41	112.57	7.03	2.15
H100 uniaxial stress	3.00	43.55	145.64	6.37	1.51
H60 uniaxial stress	3.00	43.55	145.64	3.01	1.37

4.2.1 H100 Uniaxial strain analyses

The mechanical response in tension and compression generally has good match with experimental data for the uniaxial strain analyses, see Figures 4.3a and 4.3b. In the elastic region the response is captured very accurately, and in compression the buckling as well as the initial post buckling behaviour is captured. For tension in the 3-direction local yielding occurs at around 1.5% strain which rapidly propagates throughout the faces causing an abrupt softening at around 2% strain. To avoid this phenomenon, the yield stress would have to be raised to a nonphysical level which would cause bad results in compression. The response in the 3-direction for tension was therefore only optimised until 2%, as was briefly mention in Section 3.5.

Since the boundary conditions do not allow for transverse contractions, the global Poisson's ratio is not accurately captured. With an incorrect global Poisson's ratio the global shear modulus is not correct causing the shear response to be off by a factor of 2 in the 1-direction as seen in Figure 4.3c. To capture the shear response the RVE must hence be able to contract and expand transversely when exposed to tension and compression making uniaxial stress favourable.

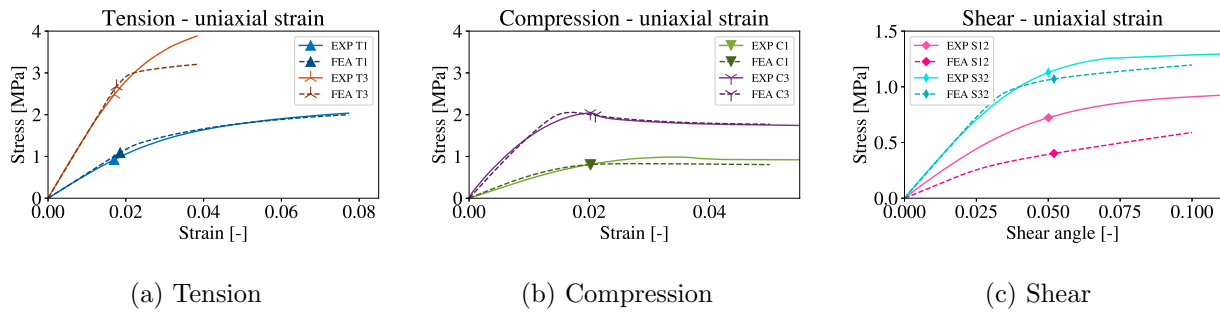


Figure 4.3: H100 Stress-strain results for uniaxial strain analyses

From the local stress plots in Figures 4.4 through 4.6 it can be observed that all analyses show local yield in some area with stresses surpassing the yield stress. Although tension in the 3-direction has the lowest local maximum stress, Figure 4.4b, the stress is more evenly distributed, allowing for a larger amount of elements to yield simultaneously causing the abrupt softening seen in Figure 4.3a. This problem does not occur for tension in the 1-direction, Figure 4.4a, where the local stresses in the hexagonal faces are substantially lower. This analyses does however show the highest local stress confined to the corners of the quadrilateral faces increasing the risk for local fracture.

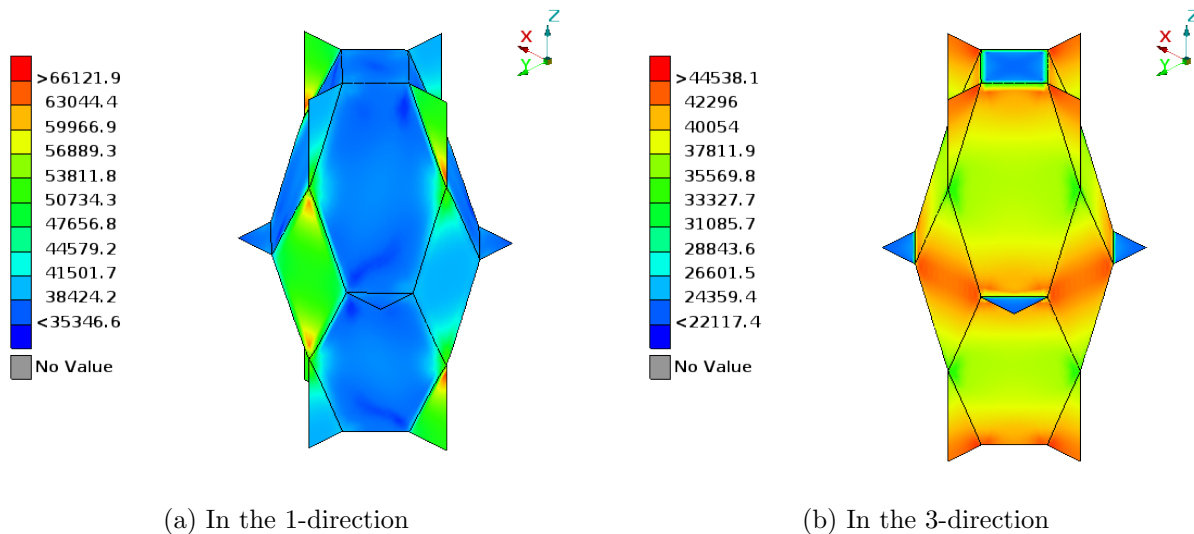


Figure 4.4: H100 Uniaxial strain tension - σ_{vM} on deformed model [kPa]

In compression the buckling is observed both in the deformation of the geometry and in the local stress distribution, see Figure 4.5. The highest local stresses are confined to the buckled region of the geometry making these areas critical.

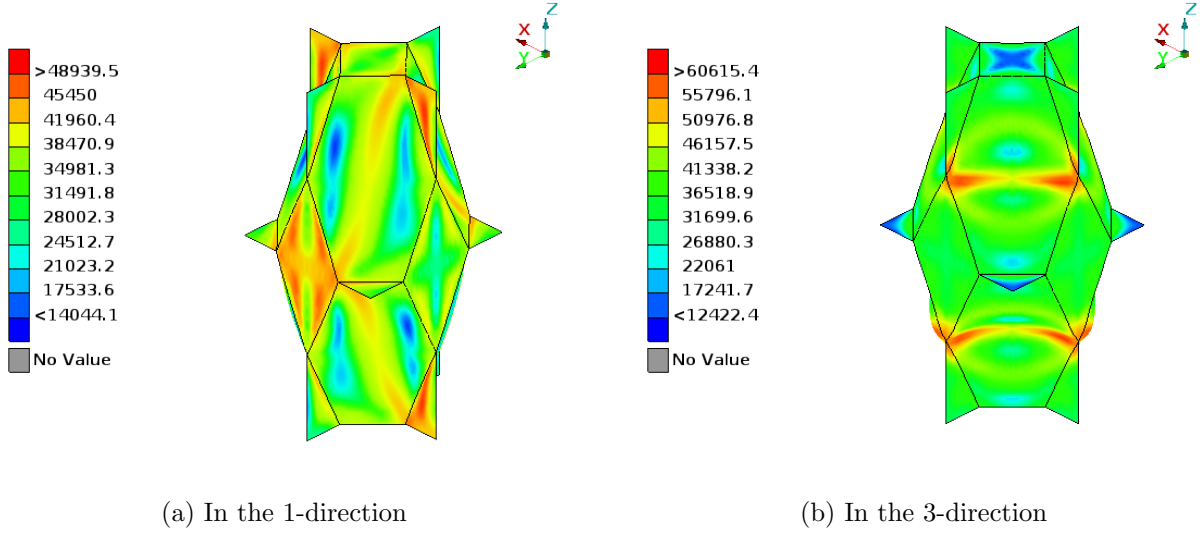


Figure 4.5: H100 Uniaxial strain compression - σ_{vM} on deformed model [kPa]

The shear deformation is hard to observe in the 12-direction, but is more pronounced in the 32-direction, see Figure 4.6. The stress distribution is more evenly distributed for shear in the 32-direction while shear in the 12-direction has a slightly higher peak stress.

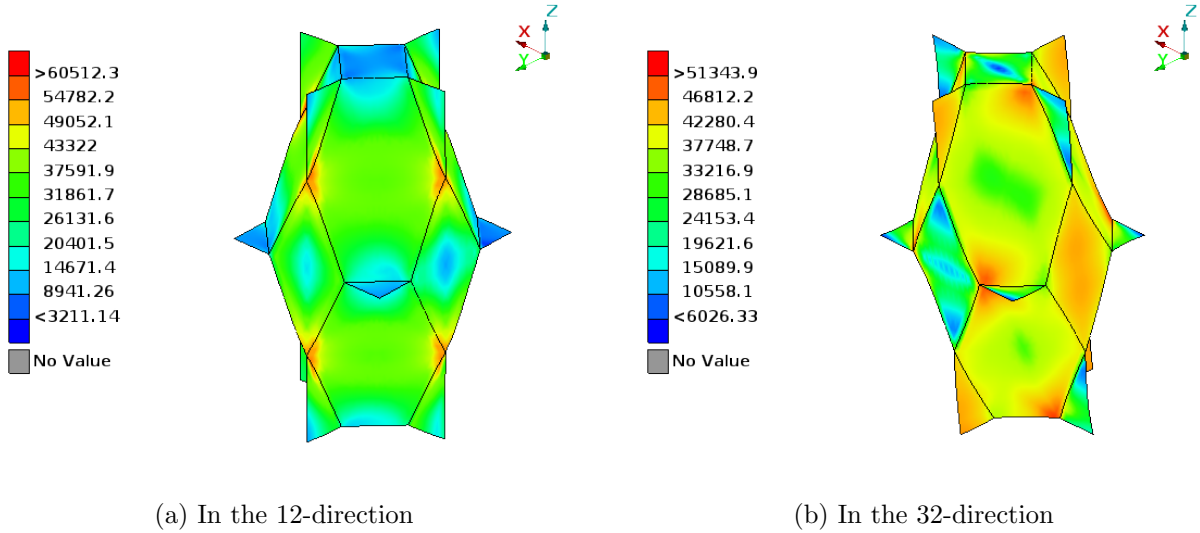


Figure 4.6: H100 Uniaxial strain shear - σ_{vM} on deformed model [kPa]

Noteworthy for all local stress plots is that the deformation, as well as the local stresses, are completely repeatable on all faces and edges. If one cell were to be repeated in all directions, four triangular faces would comprise one quadrilateral face with the same local stresses as those observed in the already existing quadrilateral faces. This is a good indication that the PBC's are working as intended.

4.2.2 H100 Uniaxial stress analyses

For the analyses performed under macroscopic uniaxial stress conditions, the elastic region is captured in a decent manner for all analyses, see Figure 4.7. The boundary conditions for uniaxial stress are

less stiff than for uniaxial strain, making it necessary to compensate for the loss of stiffness with a higher Young's modulus. Since the strain response is captured a great deal better with uniaxial stress these results are more consistent than the results from uniaxial strain. In tension, the FE data displays a larger degree of softening after yield than the experimental data, causing the stresses to be underestimated. The critical buckling load is captured better for compression in the 3-direction than for compression in the 1-direction. However, the general match between FE and experimental data is better for the latter loading direction. For the shear analyses in the 32-direction, the FE data yields more critically, similar to the FE tension data in the 3-direction, and is therefore not able to capture both the elastic and plastic regions of the experimental data simultaneously.

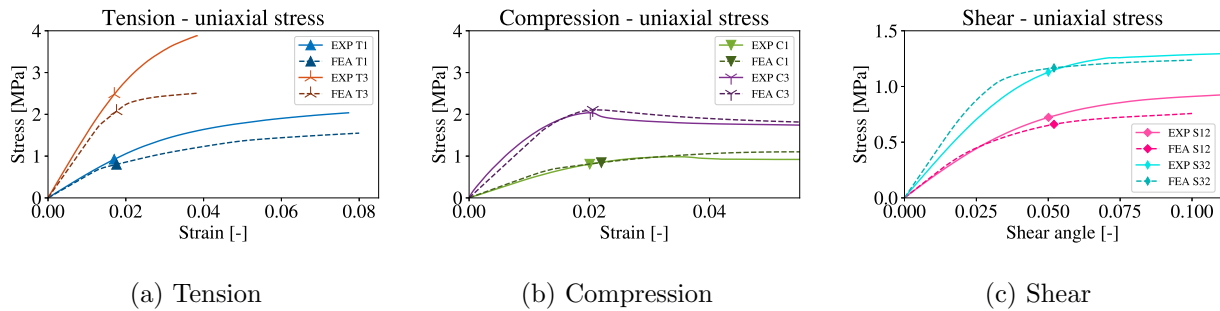


Figure 4.7: H100 Stress-strain results for uniaxial stress analyses

The loads in the RVE during tension in the 1-direction are primarily distributed in the triangular and quadrilateral faces in the 1-2 plane, see Figure 4.8a. Not much load is distributed in the same faces in the 1-3 plane. This can be explained by the transverse contraction and the elongation of the RVE which enables it to contract more in the 3-direction than in the 2-direction. Contrarily, for tension in the 3-direction, Figure 4.8b, a greater deal of load is distributed in the hexagonal faces making the over all distribution more even in the structure.

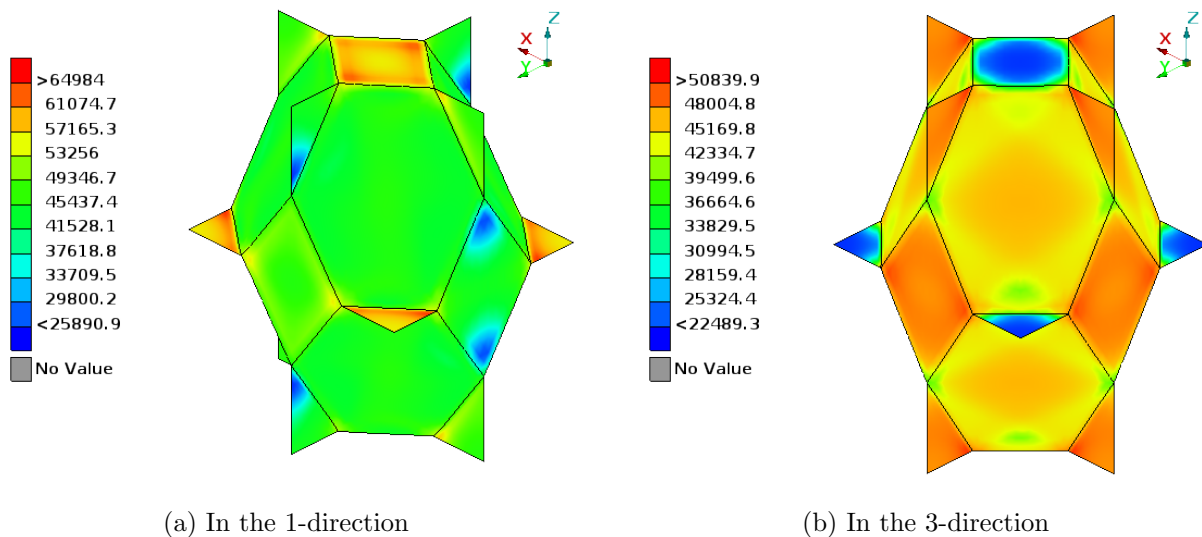
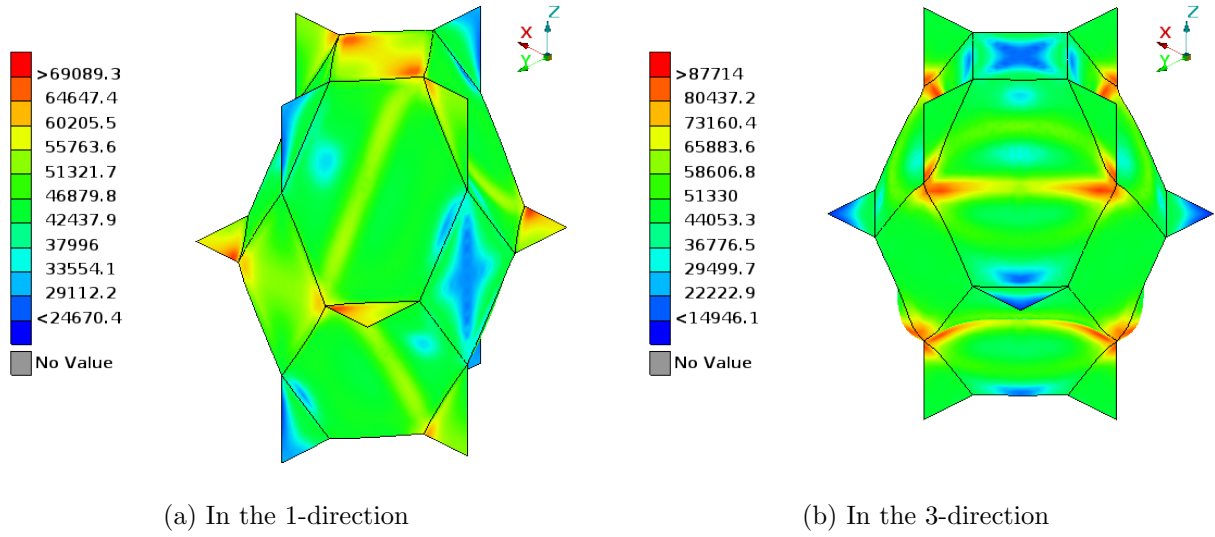
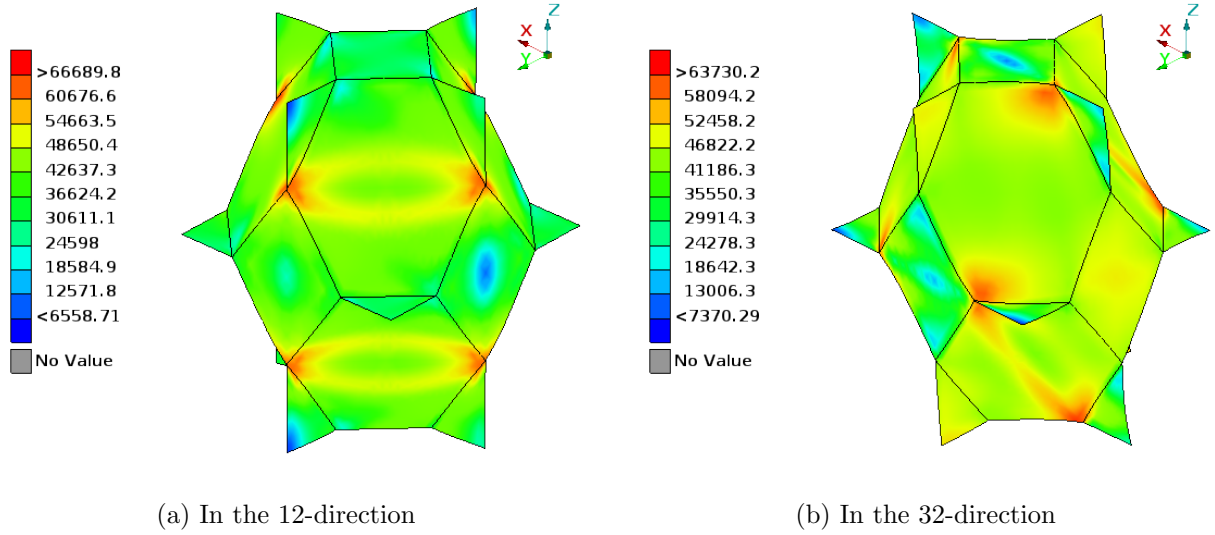


Figure 4.8: H100 Uniaxial stress tension - σ_{vm} on deformed model [kPa]

In compression, Figure 4.9, the deformation under uniaxial stress conditions is a lot similar to that of uniaxial strain, with the same buckling pattern in both the 1- and 3-direction. However, for the uniaxial stress analyses transverse contraction can be observed in the figures as it is now allowed for in the boundary conditions.

Figure 4.9: H100 Uniaxial stress compression - σ_{VM} on deformed model [kPa]

The shear analyses, Figure 4.10, show a tendency to buckle, as opposed to the shear analyses during uniaxial strain. The deformation pattern for shear in the 12-direction reflects the buckling pattern for compression in the 3-direction, while shear in the 32-direction reflects the buckling pattern in for compression in the 1-direction.

Figure 4.10: H100 Uniaxial stress shear - σ_{VM} on deformed model [kPa]

4.2.3 H60 Uniaxial stress analyses

When the geometric parameters from the uniaxial stress analyses of H100 are re-scaled to fit H60, the elastic response is captured even better for all analyses, see Figure 4.11. The stress-strain response for larger strains in tension and compression is also better than that of H100. The shear response saturates at a lower level than the experimental data providing a worse fit to the experimental data than H100 after the elastic region.

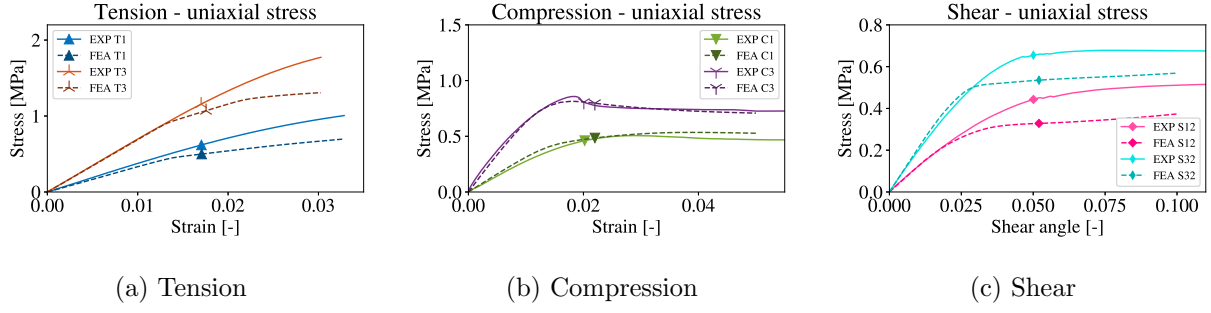
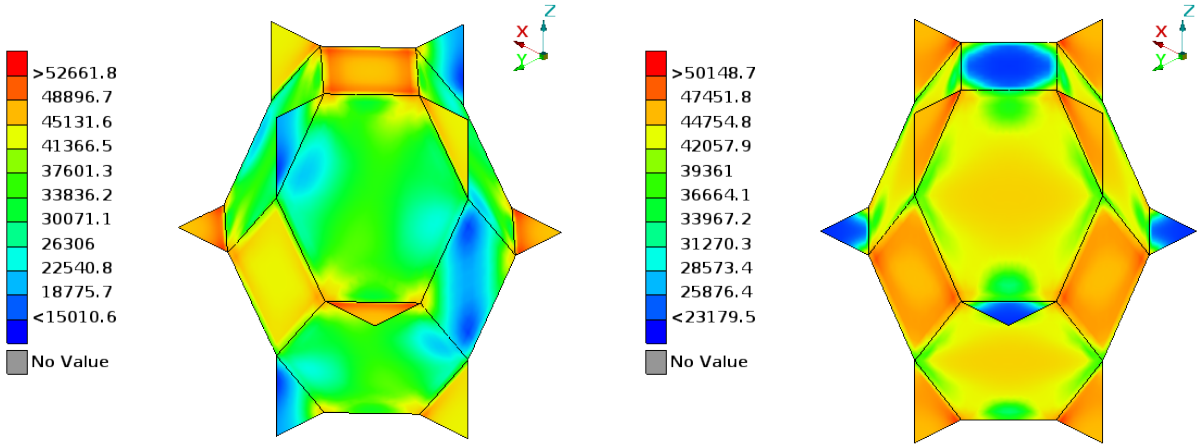
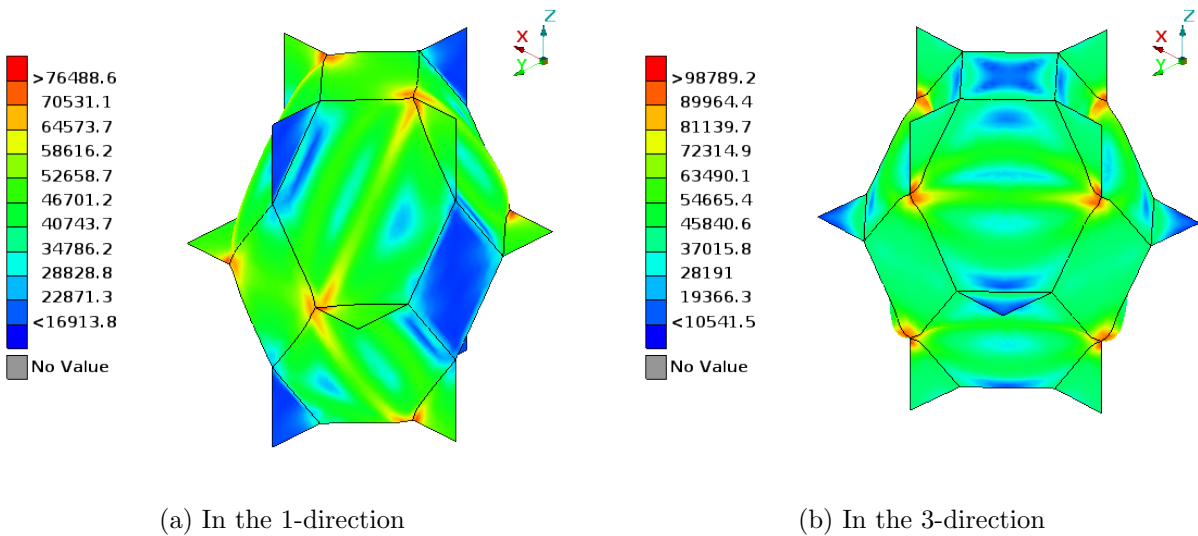
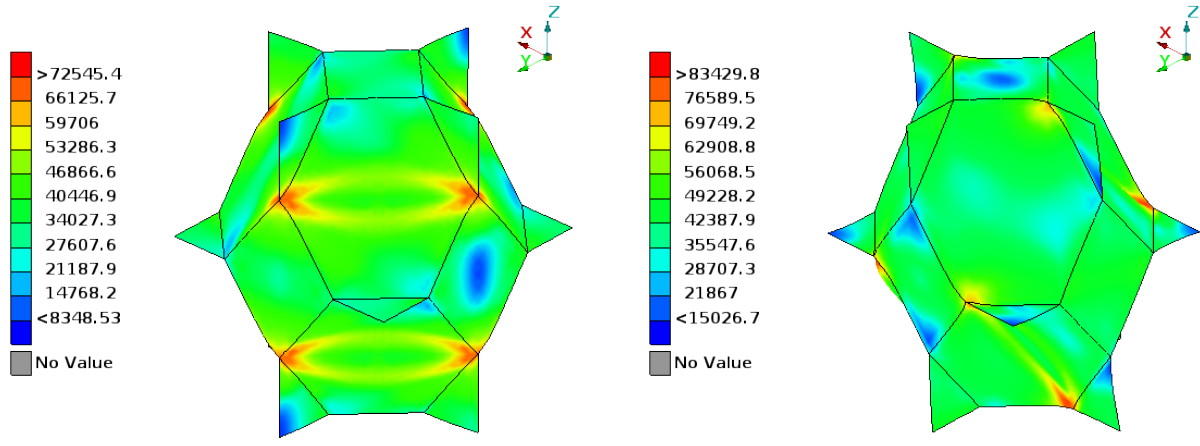


Figure 4.11: H60 Stress-strain results for uniaxial stress analyses

The deformation and local stress distribution in H60, seen in Figures 4.12 to 4.14, is also very similar to that of H100. The major difference between the two are that the distribution of stresses are less even in H60.

Figure 4.12: H60 Uniaxial stress tension - σ_{vM} on deformed model [kPa]Figure 4.13: H60 Uniaxial stress compression - σ_{vM} on deformed model [kPa]



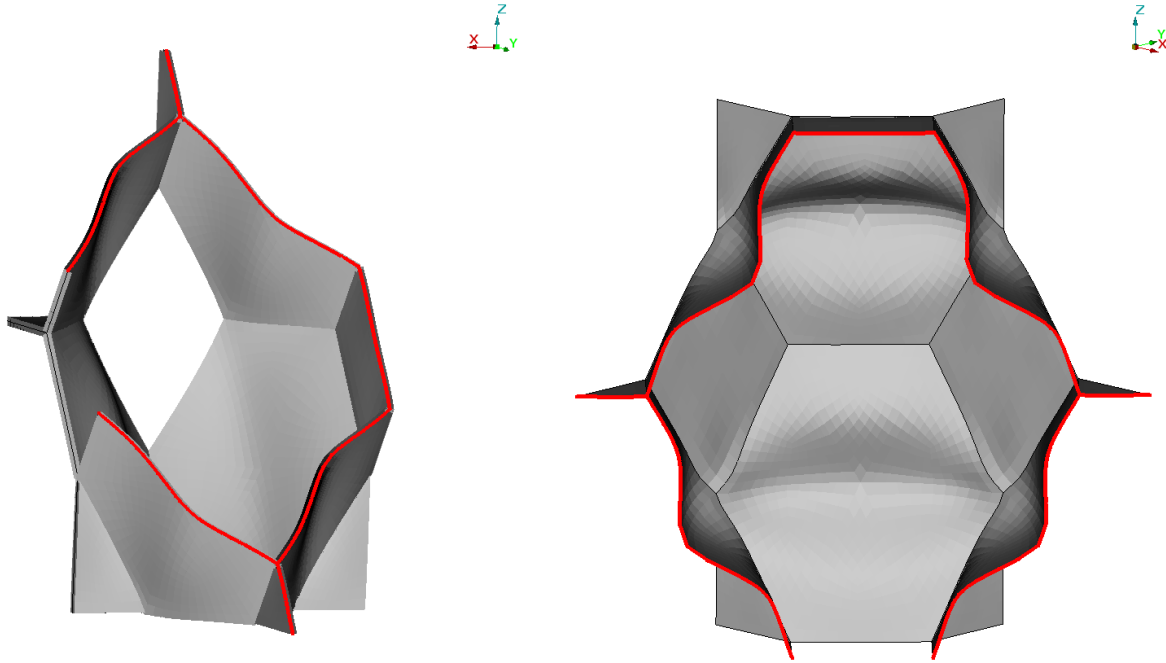
(a) In the 12-direction

(b) In the 32-direction

Figure 4.14: H60 Uniaxial stress shear - σ_{vM} on deformed model [kPa]

4.2.4 Buckling deformation

The buckling deformation from compression is illustrated in Figure 4.15 where section cuts (highlighted by red lines) have been made to better show the buckling. It can be observed that the structure buckles more critically when loaded in the 3-direction than in the 1-direction.



(a) Compression in the 1-direction

(b) Compression in the 3-direction

Figure 4.15: Section cuts of deformed geometry after buckling

4.2.5 Global material parameters

From the FEA results, the final global macroscale material parameters were calculated according to Equations (3.13) to (3.15). In the experimental data the Young's modulus in tension did not equal that in compression. Since the tensile result will have less discrepancies from local buckling of cell walls, the tensile experimental results were used for comparison in Tables 4.4 and 4.5. The Young's

moduli for the experimental data were calculated¹ from the data shown in Figures 4.3, 4.7, and 4.11, while the experimental Poisson's ratios were supplied by Diab. Even though the linear behaviour in the FE analyses did not differ between the tensile and compressive results all results shown in Tables 4.4 and 4.5 are calculated from tensile analyses to ensure comparability. The Poisson's ratios were calculated at a time step within the elastic region of the analyses.

The boundary conditions implementing uniaxial strain adds stiffness to the structure resulting in, even with a lower stiffness of the bulk material, a higher global Young's modulus than for uniaxial stress, see Table 4.4. Even though this added stiffness results in a better match of Young's modulus with experimental data, transverse contractions are not allowed for in uniaxial strain resulting in a Poisson's ratio of 0 in all directions. Contrary, the resulting shear modulus and Poisson's ratios for the uniaxial stress analyses are close to the experimental data, except for ν_{13}^* which is a bit too low.

Table 4.4: Final global parameters for the H100 analyses

H100 data	E_{11}^* [MPa]	E_{33}^* [MPa]	G_{12}^* [MPa]	G_{32}^* [MPa]	ν_{12}^* [-]	ν_{13}^* [-]	ν_{31}^* [-]	ν_{32}^* [-]
Experimental	57.56	157.05	19.13	29.94	N/A	0.22	0.42	0.42
Uniaxial strain	58.80	156.27	10.59	29.49	0	0	0	0
Uniaxial stress	53.04	133.42	20.31	38.03	0.55	0.15	0.39	0.39

When re-scaling the geometric parameters to fit H60, the resulting global parameters from the FE analysis are even closer to the experimental result, see Table 4.5. Once again with the exception of ν_{13}^* which is still a bit too low.

Table 4.5: Final global parameters for the H60 analysis

H60 data	E_{11}^* [MPa]	E_{33}^* [MPa]	G_{12}^* [MPa]	G_{32}^* [MPa]	ν_{12}^* [-]	ν_{13}^* [-]	ν_{31}^* [-]	ν_{32}^* [-]
Experimental	38.06	69.53	12.18	19.71	N/A	0.21	0.39	0.39
Uniaxial stress	32.97	68.79	12.39	21.07	0.50	0.18	0.37	0.37

¹The calculation of Young's moduli did not follow the standard for calculating stiffness from experimental results, but was calculated from the slope of the plot at a selected point in the elastic region for each experiment similarly to how it was calculated from the FEA results.

5

Discussion

The microstructure study gave an important insight to the structure of the foam and laid the basis for the initial estimation for the geometric parameters of the RVE. However, there were a lot of uncertainties in the results that are further elaborated here. Differences in the global mechanical response between simulated and experimental data, as well as the ability of the FE-model to capture the correct deformation is discussed, and whether the derived parameters are reasonable is expanded upon.

5.1 ESEM study

The results from the ESEM study were reviewed and implemented with caution. As only two-dimensional images were taken, it cannot be known if an observed cell was cut through its centre. A degree of uncertainty of the actual size of the cells is therefore introduced to the results. However, as the cells would only show their true dimensions if they were cut along their centre, and the probability of this happening is lower than the probability of them being cut in any other place, the sizes observed should underestimate the true size of the cells. Additionally, the elongation observed is also subject to a degree of uncertainty. As only the 1-3 plane was observed, and all cells are not perfectly aligned with the 3-direction, their true elongation was most likely not observed. Only cells which lay perfectly in the plane orthogonal to the observation axis would show their true elongation, and all other cells would show a smaller than actual elongation. The resulting elongation from the ESEM study is therefore most likely an underestimation of the true elongation of the cells. However, since not all cells are aligned perfectly with the 3-direction, this causes the elongation of individual cells to have a lesser impact on the global transversely isotropic behaviour of the foam. Therefore, the elongation of the RVE was less than the elongation measured in the ESEM study. Even though the absolute values from the study are uncertain, the relative differences between H60 and H100 still provided important guidance for the recalibration of the geometric parameters.

It was expected that the cells in H60 would be larger than the cells in H100, due to the lower density in H60, as it is allowed to rise for a longer period of time in the manufacturing process. However, the project found that the cells in H60 were actually smaller than those in H100. The reason for this is still unknown. However, to eliminate the risk of having studied the incorrect foams, the densities of the foams were measured and found to be correct.

5.2 Derived bulk and global parameters

The bulk material parameters derived from the optimisation procedure are all reasonable with respect to the material parameters of standard PVC. Early in the project, the Young's modulus was found to tend to very high values at the expense of reducing the uniform thickness. Therefore, the upper boundary of the Young's modulus was set to 3 GPa, which also ended up being the derived value after optimisation during uniaxial stress. A similar trend was also observed for the hardening modulus which also tended to its maximum value, which became the derived value for the uniaxial stress analyses¹.

¹The hardening modulus was controlled by defining the stress at initial yield and the stress at an additional plastic strain level. Therefore, the value of the hardening modulus parameter depends also on the yield stress. The hardening parameter in LS-OPT tended to its maximum value, but this is not the value stated as the hardening modulus H^* .

For the global material parameters, a very good match was achieved towards the experimental data. However, in the experimental data the elastic modulus differs between tension and compression in the 3-direction for both H60 and H100. This behaviour is not observed in the FE-model and cannot be captured with the current material model. However, there is also a possibility that the experimental data is flawed and the Young's modulus should, in fact, be the same in both tension and compression.

When using LS-OPT to find optimal parameters, extra care has to be taken to ensure that the chosen parameters are reasonable. In some cases the software could find several minimums for the optimisation problem, as was the case for Young's modulus and cell wall thickness. It was found that if one of the parameters were predetermined, the other could be used to compensate with until the desired response was reached. This makes it desirable to do a more in depth study of the microstructure to determine the actual thickness of the cell walls.

5.3 Deformation mechanics

The crushing behaviour of cellular foams in compression is strongly dependent on cells buckling layer by layer. This is not captured by the PBC's, which strongly limits this technique. The advantage of PBC's is that the number of elements needed is highly reduced. However, it leaves the crushing and densification unexplored, which is the larger part of the stress strain behaviour, as seen in Figure 5.1. To accurately use the results obtained in this study, one has to ensure that the amount of compression that is of interest does not transcend too far into the crushing region.

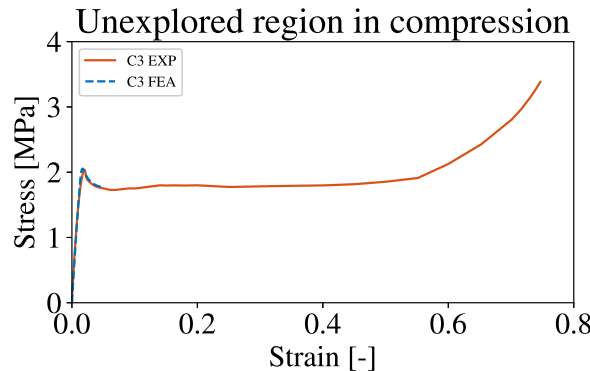


Figure 5.1: The unexplored crushing and densification in compression

Since the cell in uniaxial strain is not allowed to contract and expand in tension and compression, the mechanical response in this analysis is less affected by the elongation of the cell. To capture the transverse isotropy seen in the experimental uniaxial stress data the elongation for these analyses has to be scaled up to a factor of 2.15, compared to the elongation in uniaxial stress analyses at 1.51. Since uniaxial strain is an incorrect assumption, one can here make the argument that the parameters can be tuned to fit the experimental data regardless of previously made erroneous assumptions. This emphasises the importance of choosing accurate boundary conditions and geometry, and limiting the variable parameters within physically justifiable limits before commencing with the optimisation.

In tension there is an abrupt loss of stiffness when all elements in the quadrilateral faces yield simultaneously. To capture the gradual loss of stiffness observed in the experimental results one approach could be to implement Plateau borders, forcing the elements to plasticise in the thin elements in the centre of the face first and then gradually spread to the edges. The gradual loss of stiffness observed in the experiments could also be due to local fracture of cell walls in weaker regions of the foam. If this is the case, the current method is unable to capture this gradual softening by mimicking the actual deformation mechanism.

The experimental data aimed to be captured in the current work is obtained via uniaxial stress tests where a test specimen is bonded to load plates and subsequently loaded. This results in boundary conditions where the top and bottom of the specimen are fixed and all other surfaces are free. Therefore, the test specimen can have transverse contractions everywhere except in the loading surfaces. However, in the model developed in the current work the test specimen is a single cell with applied PBC's which either allows complete transverse contraction under uniaxial stress loads or allows no transverse contraction under uniaxial strain loads. This causes a discrepancy between the boundary conditions in the experimental tests and the developed model which has not been explored in the current work. This also raises a valid question regarding if it should be possible to properly capture the mechanical behaviour from the experimental tests using the model developed in the current work.

5.4 Element type

In the beginning of the project, elements with full integration were used. However, due to some unexpected results in the stress plots where the stress varied unevenly through the integration points in some elements, reduced integration elements were used instead. With reduced integration elements these issues were eliminated and, luckily, the global stress-strain response of the RVE stayed the same. With reduced integration hourglass effects might be encountered. This was analysed by reviewing the artificial strain energy and comparing it to the internal energy. From these results, no evidence was found that hourglass effects occurred and had to be stabilised.

5.5 Error sources

Sources of error which could have influenced the results are analysed and presented here.

5.5.1 Analysis type

The analyses were performed as Dynamic Implicit, with a small amount of material damping added for stabilisation, as this analysis type was more efficient and stable than the more accurate Riks method. This shortened the analysis time considerably when carrying out iterations to find the optimal parameters. Since the added material damping is known to be artificial, this will cause a slight error in all analyses. To verify the severity of this error a control analysis was made using Riks method. The resulting comparison is illustrated in Figure 5.2. There is no noticeable difference between the two, except for in compression in the 3-direction where the damping makes the buckling response slightly less pronounced.

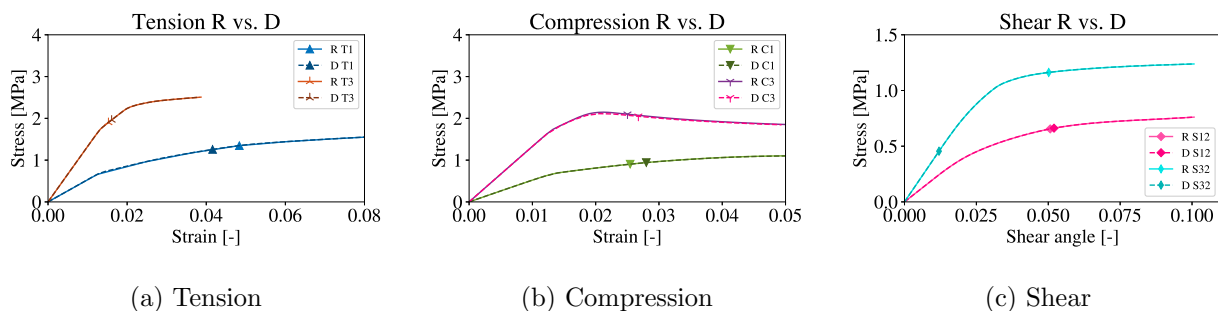


Figure 5.2: Comparison between Dynamic Implicit (D) and Riks (R) analyses

5.5.2 Influence of imperfection

The amount of imperfection added to the initial geometry was found to influence the results early in the project. Therefore, this parameter was studied further on a Dynamic Implicit analysis with 10% applied global compressive strain in the 3-direction. The imperfection is added such that the nodes of

the geometry are shifted according to the displacements from a buckling analyses. The amount a node is moved is calculated such that the nodes are moved a percentage of the element thickness. From Figure 5.3 it can be observed that the stress-strain behaviour can differ to a large extent as a result of the imperfection. For zero percent imperfection, the buckling is initiated at a higher load and is also more critical with a higher loss of stiffness. Furthermore, a secondary loss of stiffness is observed. The first loss of stiffness is due to the lower half of the RVE buckling and the second is due to the upper half buckling. At 20 percent imperfection the buckling is more controlled and with a clear loss of stiffness. At the extreme value of 200 percent imperfection, the buckling is a lot less pronounced. Furthermore, at this level of imperfection the initial elastic response has also been weakened.

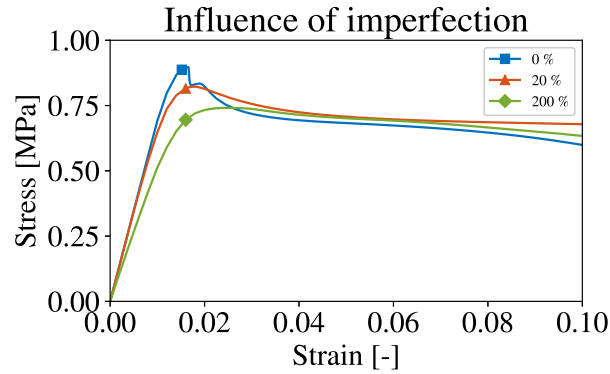


Figure 5.3: Study on the influence of the added imperfection in compression on H60

For zero percent imperfection the RVE only buckled on one side, see Figure 5.4a. This caused the local element deformations to be very high in some places, which is undesirable. At 20 percent, the RVE buckled anti-symmetrically on the upper and lower half, see Figure 5.4b. This is the wanted behaviour as the buckling is more balanced and less elements have very high amounts of deformation. At 200 percent imperfection the upper half buckled similar to the zero percent analysis. However, at the higher amount of imperfection the lower half showed a greater deal of deformation due to the very high amount of added imperfection. From these analyses it is clear that if the RVE buckles on both sides, a proper amount of imperfection has been used.

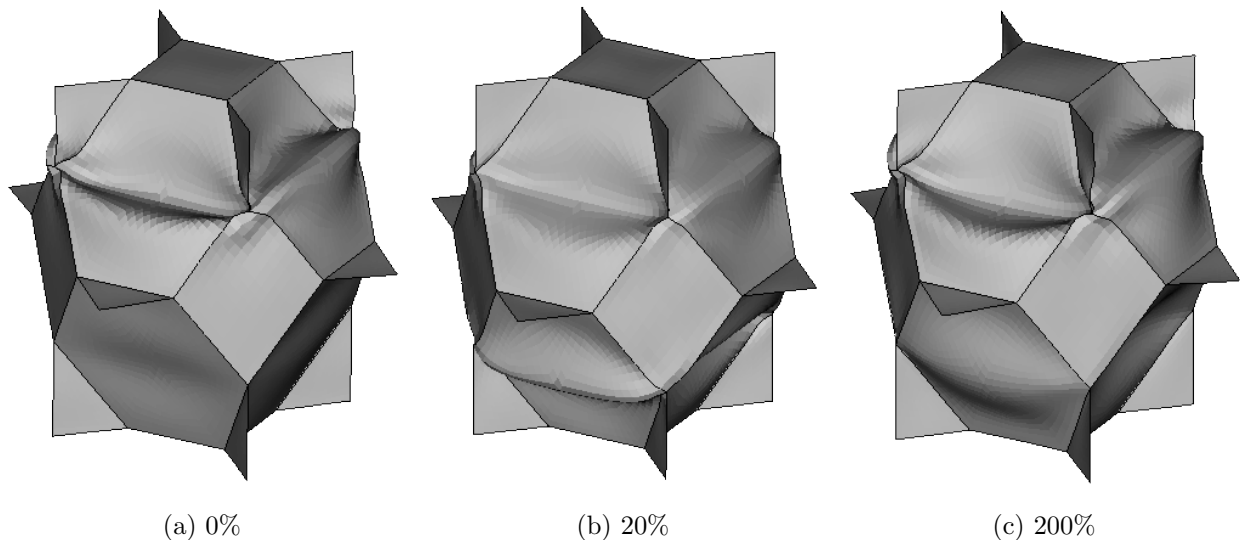


Figure 5.4: Deformed geometries with varying amounts of initial imperfection

5.5.3 Incorrect boundary conditions for shear analyses

The boundary conditions for the shear analyses were not implemented correctly for the uniaxial strain analysis. The shear analysis in uniaxial strain should be implemented in the same way as it is for shear in uniaxial stress. This could be an explanation as to why the shear responses were bad for the uniaxial strain analyses. However, this was discovered too late in the project to be rectified.

6

Conclusions

The aim of the project was to develop a finite element model that adequately captures the mechanical behaviour of Divinycell H100 and H60. It can be concluded that an RVE in the shape of a Kelvin tetrakaidecahedron can be used together with PBC's to model both the elastic and plastic mechanical response for a Divinycell H100 cellular foam by optimising material and geometric parameters. The elastic region have been captured well in both tension, compression, and shear for two principal directions. Furthermore, the compressive response has also been captured well in the immediate post-buckling region. Finally, the elastic tensile, compressive, and shear response of Divinycell H60 have also been captured well by re-scaling the geometric parameters from the H100 optimisation and keeping the derived material parameters constant. The compressive response in the immediate post-buckling region was captured well also for H60.

Although a lot of uncertainties are left regarding the optimal material and geometrical parameters, the once derived in this study are comparable with conventional PVC material parameters and observed geometric parameters in the foam.

The full deformation behaviour of foams under compression can not be captured by using an RVE with full PBC's. For foams under compression the cells buckle layer by layer whereas for the RVE with PBC's all cells are implicitly assumed to buckle simultaneously.

The cell size and shape in a foam vary to a great extent, making it difficult to determine the correct shape to be used for an RVE. Furthermore, the orientation of cells also vary a great deal, complicating the determination of RVE shape further. A noticeable difference is however measured between different types of foam, making it necessary to tailor the geometry of each RVE to the specific foam studied.

7

Future work

To get a better match to the experimental data for the analysed load cases, a change in geometry is most likely needed. This could include, e.g., adding Plateau borders instead of having uniform thickness or adding curvature from surface energy minimisation to the cell walls. These changes could help in achieving a better match for tension and shear while maintaining, or improving, the match in compression. Furthermore, adding more geometric parameters could help in differentiating the results between different foam densities. For the current model Plateau borders could be introduced by having separate thicknesses for elements with different distances to the borders between faces. This could be implemented in many different ways. For example, only one additional thickness could be introduced for the first row of elements at the borders, or for the first n rows of elements. However, several thicknesses could also be introduced and used for varying rows of elements such that the thickness decreases in steps from the boarder to the face. In Figure 7.1, the first row of elements closest to the border have been selected to have a different thickness than the rest of the faces.

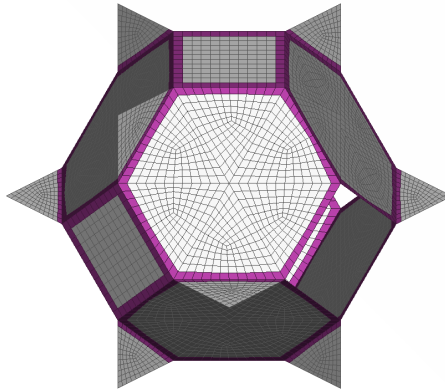


Figure 7.1: Example of implementation of Plateau borders where the first row of elements have been assigned a different thickness than the rest of the elements on the faces

Another possible way to improve the fit between the FEA data and the experimental data could be to use a different plasticity model. The linear isotropic hardening model currently used might not be advanced enough to properly capture the behaviour of the bulk material. Other plasticity models that could be used are power law hardening or a different step wise linear isotropic hardening model.

In the Kelvin RVE used in the project, the opposing quadrilateral face have been removed in order to avoid double thickness of these faces when the RVE is periodically repeated. Another remedy for this problem would be to use two opposing faces and reduce the cell wall thickness on these faces by 50%, effectively creating one face with the correct thickness upon periodic repetition. With this method the quadrilateral faces would be included in the PBC equations which theoretically should result in the same response, but this has not been proven. Opposing quadrilateral faces would result in a symmetric RVE, which could be easier to work with. For example, if the PBC's were to be verified by a model where the RVE is physically repeated in the three principal directions into a larger block of cells, the boundary effects from the non-symmetry would be avoided.

To achieve a better correlation between experimental and FEA shear data, this analyses could be included in the optimisation procedure. Although it was beneficiary to use the shear analyses to

verify the optimised parameters, including the shear analyses might provide better parameters and a better fit.

To capture the progressive buckling and densification seen in Figure 5.1, without increasing the number of elements too significantly, an FE-model with numerous cells stacked on top of each other could be used. With a slightly different imperfection in each cell, and periodic boundary conditions applied to the sides of the stack, this model would emulate a large, thin sheet of foam in which each layer would have a different tendency to buckle. This model would require self contact to be used and would still contain a large amount of elements increasing the analysis time significantly.

As a conclusion to the future work chapter it has to be mentioned that the ability to customise foams creates a myriad of foam types yet to be analysed. As an example, the latest generation of Divinycell foam can be mentioned. Although it was not included in the study, images of a sample of this foam, H60MC, was taken in the ESEM. Even though H60MC has the same density as H60 the difference in microstructure is significant, as can be seen in Figure 7.2.

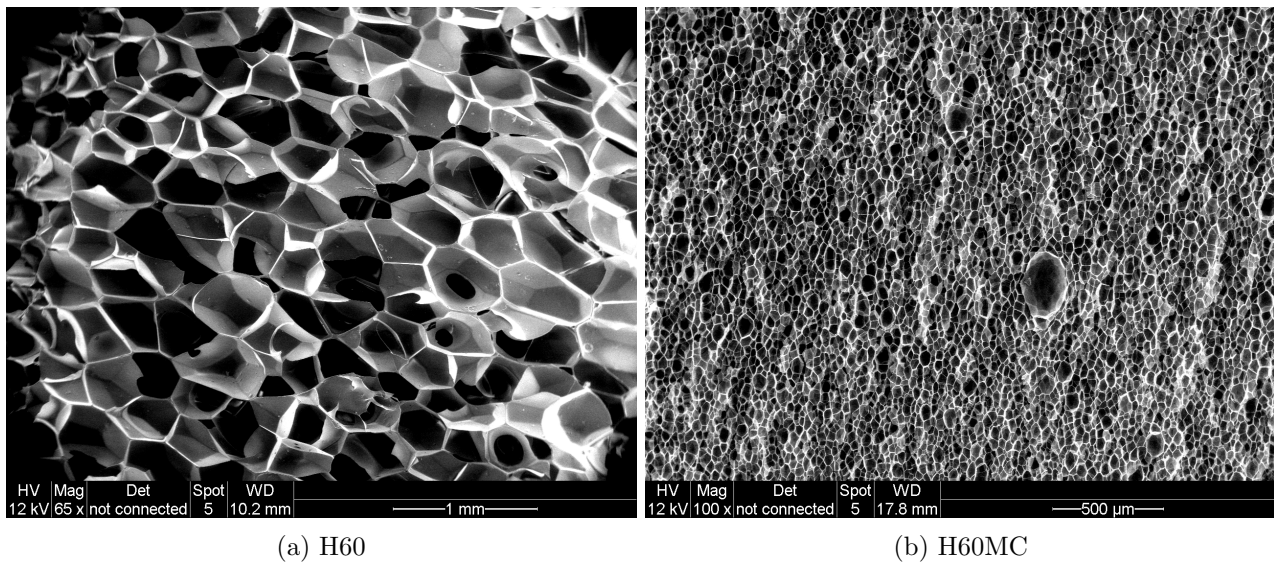


Figure 7.2: Microstructure of H60 compared to H60MC

Bibliography

- [1] R.S. Ayyagari and M. Vural. On the nature of pressure dependence in foams. *International Journal of Solids and Structures*, 78:160–173, 2016.
- [2] R.S. Ayyagari and M. Vural. Multiaxial yield surface of transversely isotropic foams: Part I—modeling. *Journal of the Mechanics and Physics of Solids*, 74:49–67, 2015.
- [3] M. Shafiq, R.S. Ayyagari, M. Ehaab, and M. Vural. Multiaxial yield surface of transversely isotropic foams: Part II—experimental. *Journal of the Mechanics and Physics of Solids*, 76: 224–236, 2015.
- [4] T. Daxner, R.D. Bitsche, and H.J. Böhm. Space-filling polyhedra as mechanical models for solidified dry foams. *Materials transactions*, 47(9):2213–2218, 2006.
- [5] M.S. Rajput, M. Burman, J. Köll, and S. Hallström. Compression of structural foam materials—experimental and numerical assessment of test procedure and specimen size effects. *Journal of Sandwich Structures & Materials*, 21(1):260–288, 2019.
- [6] C.J. Lindholm. Personal communication, 2019. 2019-04-09, Gothenburg.
- [7] L. Gigliotti and S.T. Pinho. Prediction of the post-crushing compressive response of progressively crushable sandwich foam cores. *Composites Part A: Applied Science and Manufacturing*, 80:148–158, 2016.
- [8] V.S. Deshpande and N.A. Fleck. Multi-axial yield behaviour of polymer foams. *Acta materialia*, 49(10):1859–1866, 2001.
- [9] P. Poapongsakorn and L.A Carlsson. Fracture toughness of closed-cell pvc foam: Effects of loading configuration and cell size. *Composite Structures*, 102:1–8, 2013.
- [10] M. Colloca, G. Dorogokupets, N. Gupta, and M. Porfiri. Mechanical properties and failure mechanisms of closed-cell pvc foams. *International journal of crashworthiness*, 17(3):327–336, 2012.
- [11] A.E. Simone and L.J. Gibson. Effects of solid distribution on the stiffness and strength of metallic foams. *Acta Materialia*, 46(6):2139–2150, 1998.
- [12] J. Köll and S. Hallström. Elastic properties of equilibrium foams. *Acta Materialia*, 113:11–18, 2016.
- [13] J.A.F. Plateau. *Statique expérimentale et théorique des liquides soumis aux seules forces moléculaires*, volume 2. Gauthier-Villars, 1873.
- [14] W. Thomson. On the division of space with minimum partitional area. *Acta Math.*, 11:121–134, 1887. doi: 10.1007/BF02612322.
- [15] D. Weaire and R. Phelan. A counter-example to kelvin’s conjecture on minimal surfaces. *Philosophical Magazine Letters*, 69(2):107, 1994. ISSN 09500839.
- [16] B. Buffel, F. Desplentere, K. Bracke, and I. Verpoest. Modelling open cell-foams based on the weaire–phelan unit cell with a minimal surface energy approach. *International Journal of Solids and Structures*, 51(19-20):3461–3470, 2014.

- [17] A.P. Roberts and E.J. Garboczi. Elastic moduli of model random three-dimensional closed-cell cellular solids. *Acta materialia*, 49(2):189–197, 2001.
- [18] K. Brakke. Surface evolver manual. *Mathematics Department, Susquehanna Univerisity, Selinsgrove, PA*, 17870(2.24):20, 1994.
- [19] Dassault Systèmes. *Abaqus Analysis User’s Guide*, 6.14 edition, 2014.
- [20] Livermore Software Technology Corporation. *LS-DYNA KEYWORD USER’S MANUAL: Volume II - Material models*, r11.0 edition, 2018.
- [21] E. Riks. An incremental approach to the solution of snapping and buckling problems. *International journal of solids and structures*, 15(7):529–551, 1979.
- [22] N. Vassios. Nonlinear analysis of structures, 2015.
- [23] W. Wu, J. Owino, A. Al-Ostaz, and L. Cai. Applying periodic boundary conditions in finite element analysis. In *SIMULIA Community Conference, Providence*, pages 707–719, 2014.
- [24] K. Brakke. The surface evolver. *Experimental mathematics*, 1(2):141–165, 1992.
- [25] BETA CAE SYSTEMS - ANSA, VERSION 18.1.1. <https://www.beta-cae.com/ansa.htm>, 2019. Accessed: 2019-01-29.
- [26] V. Tita, M.F. Caliri, R.A. Angelico, and R.B. Canto. Experimental analyses of the poly (vinyl chloride) foams’ mechanical anisotropic behavior. *Polymer Engineering & Science*, 52(12):2654–2663, 2012.
- [27] Imagej. <https://imagej.nih.gov/ij>, 2019. Accessed: 2019-03-05.
- [28] Morpholibj. <https://imagej.net/MorphoLibJ>, 2019. Accessed: 2019-03-05.
- [29] N. Stander, W. Roux, T. Eggleston, and K. Craig. Ls-opt user’s manual—a design optimization and probabilistic analysis tool for the engineering analyst. *Livermore Software Technology Corporation, Livermore*, 2007.
- [30] Matweb - pvc, extruded. <http://www.matweb.com/search/DataSheet.aspx?MatGUID=bb6e739c553d4a34b199f0185e92f6f7&ckck=1>, 2019. Accessed: 2019-03-25.

Appendix

A.1 PBC Matlab code

```
%%%%%%%%%%%%%%%%%%%%%%%%%%%%%%%%%%%%%%%%%%%%%%%%%%%%%%%%%%%%%%%%%%%%%%%%%%%%%%
% Script that finds opposite nodes of a 3D cubc RVE and writes an Abaqus
% inputfile with specified PBC.
% Input .txt files should include % NodeID,X,Y,Z with one headerline
%
% Dummy set and nodes are needed as *Equation has to equal 0
% Equation definition:
%   *Equation
%   Number_of_variables
%   NodeID1, dof, constant, NodeID2, dof, constant, dummynode, dof, constant
% This yields the quation:
%   NodeID1_dof*constant + NodeID2_dof*constant + dummynode_dof*constant = 0
%
% Written by Adam Billberg and Rikard Berg
%%%%%%%%%%%%%%%%%%%%%%%%%%%%%%%%%%%%%%%%%%%%%%%%%%%%%%%%%%%%%%%%%%%%%%%%%%%%%%
clear;clc
num=0;
%% Inputs
% input{num,2}='name1.txt'; Name of text file 1 for pair num
% input{num,1}='name2.txt'; Name of text file 2 for pair num
% input{num,3}=[];          dummy node number with correct sign for PBC

% Output directory
out_dir='/PBC';

% Output file name
filename='PBC.inp';

%%% Faces:
% Pair 1
num=num+1;
input{num,1}='top.txt';
input{num,2}='bot.txt';
input{num,3}=[-2];

% Pair 2
num=num+1;
input{num,1}='left.txt';
input{num,2}='right.txt';
input{num,3}=[1];

% Pair 3
num=num+1;
input{num,1}='front.txt';
input{num,2}='back.txt';
input{num,3}=[-3];

%%% Edges:
% Pair 4
num=num+1;
```

```

input{num,1}='e2.txt';
input{num,2}='e1.txt';
input{num,3}=[1, 3];

%Pair 5
num=num+1;
input{num,1}='e3.txt';
input{num,2}='e1.txt';
input{num,3}=[1];

%Pair 6
num=num+1;
input{num,1}='e4.txt';
input{num,2}='e1.txt';
input{num,3}=[3];

%Pair 7
num=num+1;
input{num,1}='e6.txt';
input{num,2}='e5.txt';
input{num,3}=[2, 3];

% Pair 8
num=num+1;
input{num,1}='e7.txt';
input{num,2}='e5.txt';
input{num,3}=[3];

%Pair 9
num=num+1;
input{num,1}='e8.txt';
input{num,2}='e5.txt';
input{num,3}=[2];

% Pair 10
num=num+1;
input{num,1}='e10.txt';
input{num,2}='e9.txt';
input{num,3}=[1, 2];

% Pair 11
num=num+1;
input{num,1}='e11.txt';
input{num,2}='e9.txt';
input{num,3}=[1];

% Pair 12
num=num+1;
input{num,1}='e12.txt';
input{num,2}='e9.txt';
input{num,3}=[2];

%% %% Start script
% Output filename
outputfilename = strcat(out_dir,filename);

fileID = fopen(outputfilename,'w');
for i_outer=1:size(input,1)

    %% Data
    % Side 1
    fid=fopen(strcat(out_dir,input{i_outer,1}));
    data=textscan(fid, '%f,%f,%f,%f','Headerlines',1);
    fclose(fid);

```

```

S1=[data{1,1}(1:end),data{1,2}(1:end),data{1,3}(1:end),data{1,4}(1:end)];
% Side 2
fid=fopen(strcat(out_dir,input{i_outer,2}));
data=textscan(fid, '%f,%f,%f,%f','Headerlines',1);
fclose(fid);
S2=[data{1,1}(1:end),data{1,2}(1:end),data{1,3}(1:end),data{1,4}(1:end)];
pre_val = input{i_outer,3}; % Prescribed value

% Check that input has same number of nodes
if length(S1(:,1))~=length(S2(:,1))
    error('Length of input not equal')
    break
end

% Define dummynodes
dummynode=[999991 999992 999993];

% Check which plane nodes are on
ind_test=[1 2 3];
tester=zeros(1,3);
for i=1:size(S1,1)-1
    for ii=1:3
        if abs(S1(i,ii+1)-S1(i+1,ii+1))<0.01
            tester(1,ii)=tester(1,ii) + 1.0;
        end
    end
end
[~,pos]=max(tester);
ind_test(pos)=[]; % Will contain the two indices which define the plane

% Get node pairs
NP=zeros(size(S1,1),2);
for i=1:size(S1,1)
    % Get distance between nodes
    diff=(ones(size(S1,1),1)*S1(i,ind_test+1) - S2(:,ind_test+1));
    dist=sqrt(sum(abs(diff).^2,2));
    [~,sorted]=sort(dist);

    % Arrange sorted nodes in array called NP
    NP(i,1)=S1(i,1);
    NP(i,2)=S2(sorted(1),1);
    S2(sorted(1),ind_test+1)=[99999 99999];
    if isempty(S2)
        break
    end
end

dummys=input{i_outer,3};
%%% Write Abaqus file
if i_outer==1 % Print dummynode info
    % Define dummynodes
    fprintf(fileID, '*Node\n');
    for i=1:length(dummynode)
        fprintf(fileID, '%.0f, 0.5, 1.1, 0.5 \n',dummynode(i));
    end
    % Define set of dummynode
    fprintf(fileID, '*NSET, NSET=%s \n','dummy_set_1');
    fprintf(fileID, '%.0f \n',dummynode(1));
    fprintf(fileID, '*NSET, NSET=%s \n','dummy_set_2');
    fprintf(fileID, '%.0f \n',dummynode(2));
    fprintf(fileID, '*NSET, NSET=%s \n','dummy_set_3');
    fprintf(fileID, '%.0f \n',dummynode(3));
    fprintf(fileID, '\n*\n');
end

```

```

% Define equations in all directions
fprintf(fileID, '*Equation\n');
for i=1:size(NP,1)
    %%% Equations with dummy nodes

    %           Equations
    for dof=1:6
        fprintf(fileID, '%g\n', length(dummys)+2);
        fprintf(fileID, '%g, %g, %g, ', NP(i,1), dof, 1);
        fprintf(fileID, '%g, %g, %g, ', NP(i,2), dof, -1);
        for dums = 1:length(dummys)
            fprintf(fileID, '%g, %g, %.1f ', ...
                dummys(dums), dof, sign(dummys(dums)));
            if dums < length(dummys)
                fprintf(fileID, ', ');
            end
        end
        fprintf(fileID, '\n');
    end
end
end

% Close file
fclose(fileID);

%%% End script

```

A.2 Python code used to extract stresses and strains

```
from abaqusConstants import *
from odbAccess import *
import sys

cur_dir = os.getcwd()

def get_results(name):
    # Define results file name and odb name
    # add current dir and add the strings
    odb_name = name + ".odb"
    output = name + ".csv"

    fullOdb = cur_dir + "\\ " + odb_name

    # Open odb file
    odb=openOdb(path=fullOdb,readOnly=True)

    # Create/open results file
    fid = open(output, 'w')
    fid2 = open('testST1.csv', 'w')

    # Get data
    mystep = odb.steps['Dynamic_load']
    region = mystep.historyRegions['Node PART-1-1.999991']
    Udata = region.historyOutputs['U1'].data
    RFdata = region.historyOutputs['RF1'].data
    TopLeftNode = (odb.steps['Dynamic_load'].frames[0].fieldOutputs['S']
        .values[0].instance.getNodeFromLabel(846).coordinates)
    BotRightNode = (odb.steps['Dynamic_load'].frames[0].fieldOutputs['S']
        .values[0].instance.getNodeFromLabel(1435).coordinates)

    U = []
    RF = []
    # Get correct units
    major = abs(TopLeftNode[2]-BotRightNode[2])
    minor = abs(TopLeftNode[0]-BotRightNode[0])
    Umult = 1/(minor)
    RFmult = 1/(minor*major*1e-6) * 1e-3 * 1e-6
    fid2.write('%0.6f , %0.6f' % (minor, major))

    for Us in Udata:
        U.append((Us[1])*Umult)

    for RFs in RFdata:
        RF.append((RFs[1])*RFmult)

    for i in range(len(RF)):
        fid.write('%0.6f , %0.6f \n' % (U[i], RF[i])) # Write to file

    odb.close()
    fid.close()
    fid2.close()

if __name__ == '__main__':
    # Map command line arguments to function arguments.
    get_results(*sys.argv[1:])
```

A.3 Example input file

```
*HEADING

**
**
**
*PARAMETER
t = .006365506
E =      3.e6
Y = 43546.3284
H = 1499989.07
L = 1.50701883
*NODE

**
** MEMBRANE and STRUCTURAL ELEMENTS
**
*ELEMENT, TYPE=S4R, ELSET=P1;Default Property

**
** SECTION DATA
**
*SHELL SECTION, ELSET=P1;Default Property, MATERIAL=M2;PVC.pl, SECTION INTEGRATION=GAUSS
<t>,      5
**
** EQUATIONS
**
*EQUATION

**
** MATERIALS
**
**
**M2;PVC.pl
**
*MATERIAL, NAME=M2;PVC.plastic
*DENSITY
1.2E-6,
*ELASTIC, TYPE=ISOTROPIC
<E>,      0.35
*PLASTIC, HARDENING=ISOTROPIC
<Y>,      0.,      0.      <H>,      10.,      0.
*DAMPING, ALPHA=0., BETA=0.0001, COMPOSITE=0., STRUCTURAL=0.
**
** AMPLITUDES
**
*AMPLITUDE, NAME=A1;amp, DEFINITION=TABULAR, VALUE=RELATIVE, TIME=STEP TIME, SMOOTH=0.25
0.,      0.,      1.,      1.
**
** SETS
**
*NSET, NSET=setname

**
*NMAP, NSET=all, TYPE=SCALE, DEFINITION=NODES
1648,
1, 1, <L>
**
*IMPERFECTION, FILE=H100-B3-6912Q-Szmap1p55-CT-P-PBC7, STEP=1
3, 8.62e-4
```

```

**
*BOUNDARY, FIXED
    1737,      1,      3
**
** STEPS
**
** STEP 1
**
*STEP, NAME=Dynamic_load, INC=200, NLGEOM=YES
*DYNAMIC, APPLICATION=QUASI-STATIC
0.02,      1.,      1.E-5,      0.02
**
** BOUNDARY
**
*BOUNDARY, TYPE=DISPLACEMENT, AMPLITUDE=A1; amp
dummy_set_3,      3,      ,      -0.0372
*OUTPUT, FIELD, FREQUENCY=2, VARIABLE=PRESELECT
*OUTPUT, HISTORY, FREQUENCY=1, VARIABLE=PRESELECT
*NODE OUTPUT, NSET=dummy_set_1
RF,
U,
*NODE OUTPUT, NSET=dummy_set_2
RF,
U,
*NODE OUTPUT, NSET=dummy_set_3
RF,
U,
*END STEP

```

A.4 Images from ESEM microstructure study

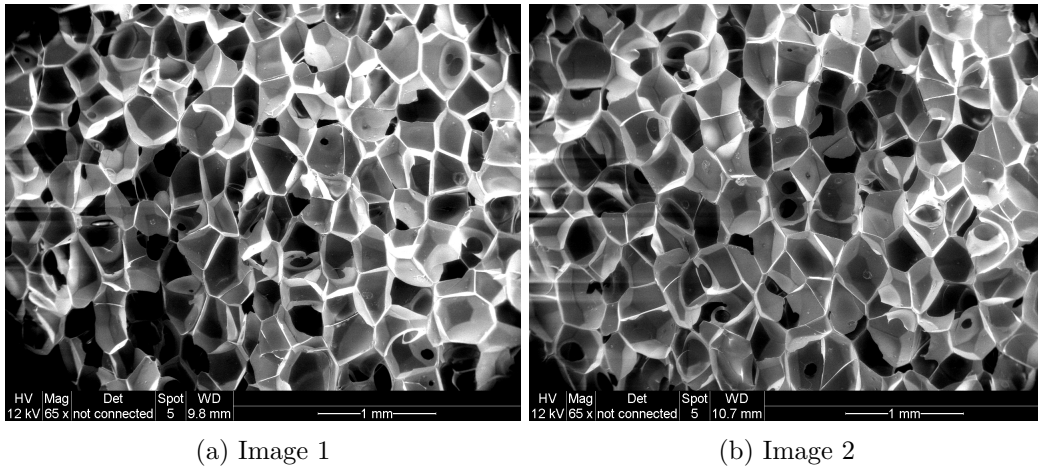


Figure A.3: H60 Plane 1

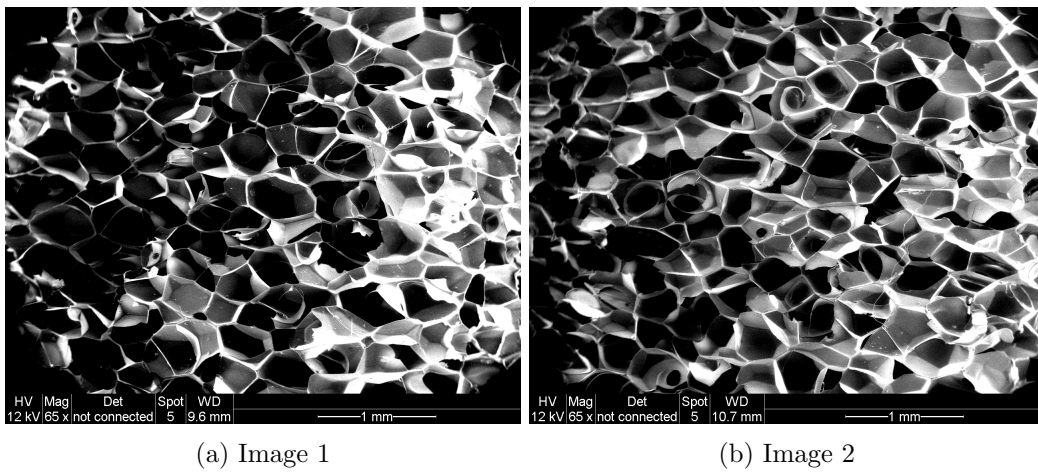


Figure A.4: H60 Plane 2

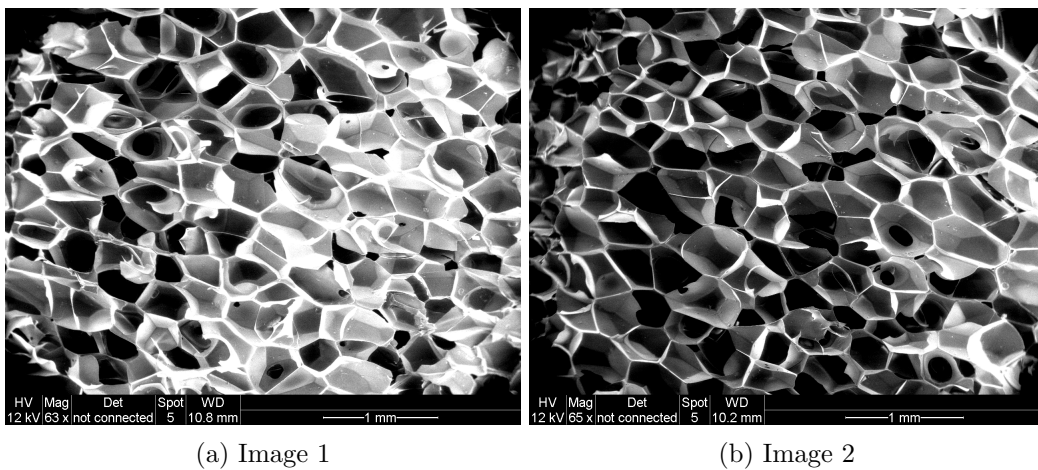
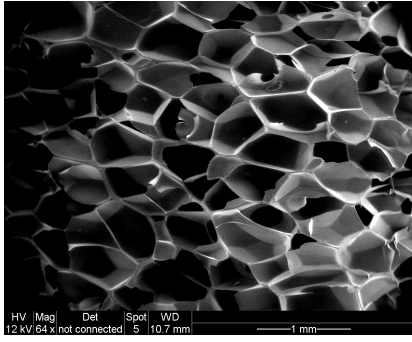
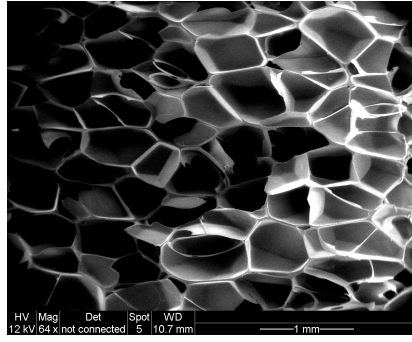


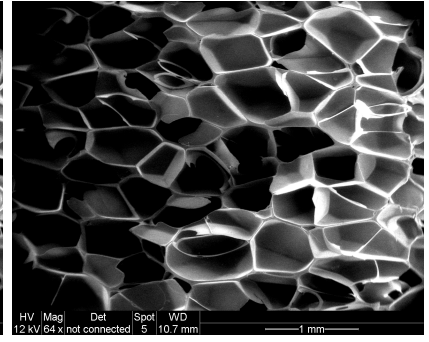
Figure A.5: H60 Plane 3



(a) Image 1

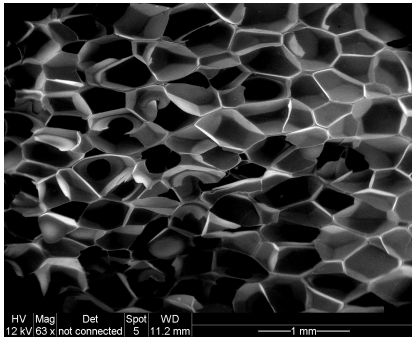


(b) Image 2

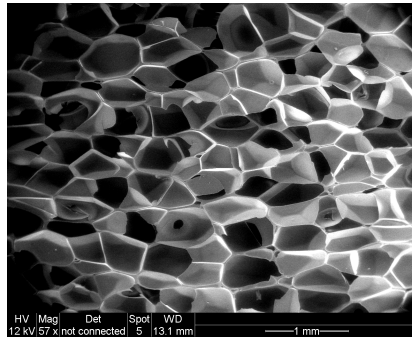


(c) Image 3

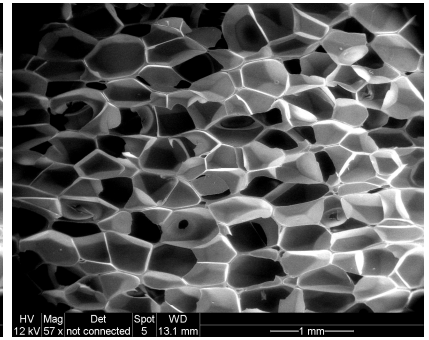
Figure A.6: H100 Plane 1



(a) Image 1

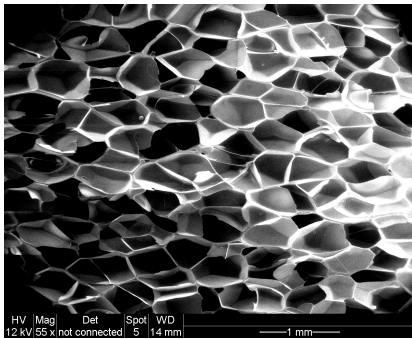


(b) Image 2

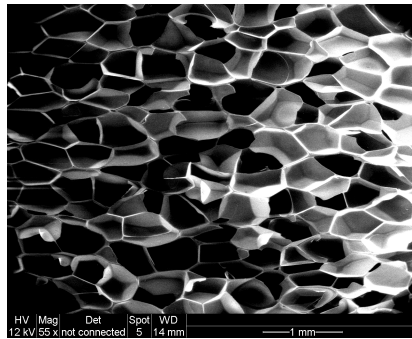


(c) Image 3

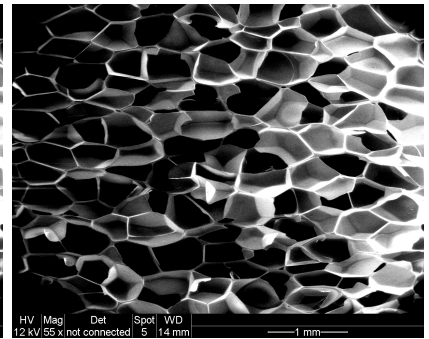
Figure A.7: H100 Plane 2



(a) Image 1

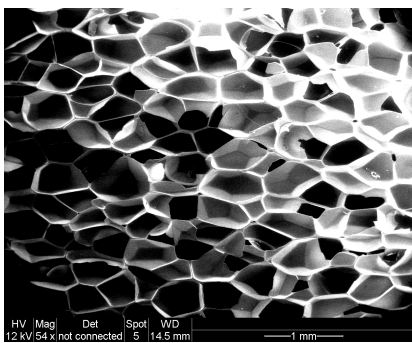


(b) Image 2

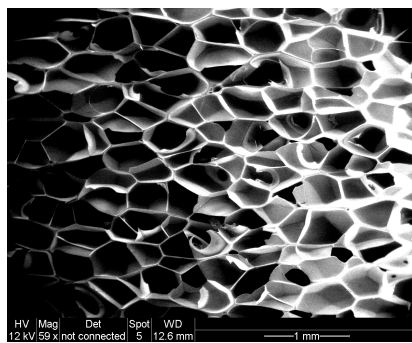


(c) Image 3

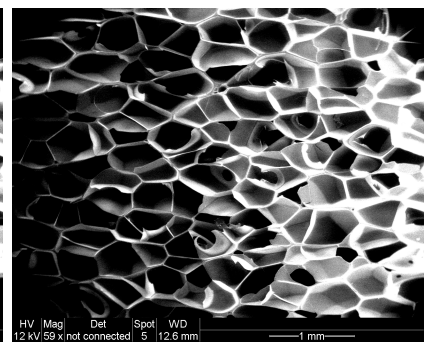
Figure A.8: H100 Plane 3



(a) Image 1

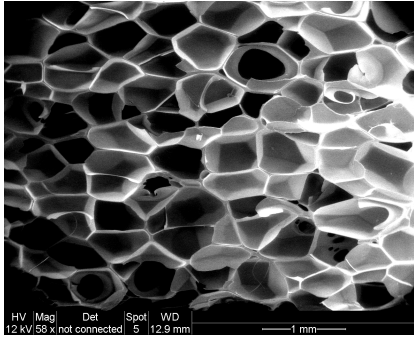


(b) Image 2

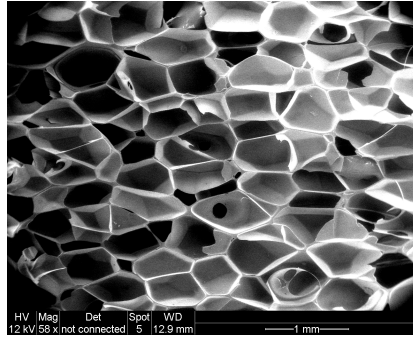


(c) Image 3

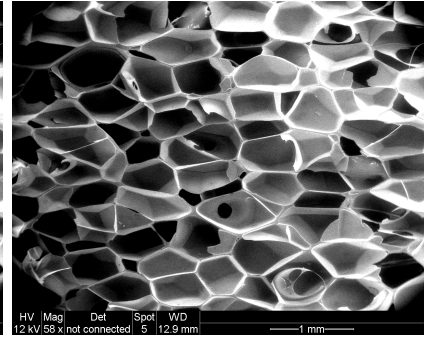
Figure A.9: H100 Plane 4



(a) Image 1



(b) Image 2



(c) Image 3

Figure A.10: H100 Plane 5